Tropical Upper Tropospheric Potential Vorticity Intrusions During Sudden Stratospheric Warmings

JOHN R. ALBERS, *

Cooperative Institute for Research in the Environmental Sciences, University of Colorado Boulder

Physical Sciences Division, NOAA Earth System Research Laboratory, Boulder, Colorado

GEORGE N. KILADIS

Physical Sciences Division, NOAA Earth System Research Laboratory, Boulder, Colorado

THOMAS BIRNER

Department of Atmospheric Science

Colorado State University, Fort Collins, Colorado

JULIANA DIAS

Cooperative Institute for Research in the Environmental Sciences, University of Colorado Boulder

Physical Sciences Division, NOAA Earth System Research Laboratory, Boulder, Colorado

* *Corresponding author address:* John R. Albers, CIRES, University of Colorado 216 UCB, Boulder, CO 80309.

E-mail: john.albers@noaa.gov

ABSTRACT

We examine the intrusion of lower stratospheric extratropical potential vorticity into the tropical upper troposphere in the weeks surrounding the occurrence of sudden stratospheric warmings (SSWs). Our analysis reveals that SSW-related PV intrusions are significantly stronger, penetrate more deeply into the tropics, and exhibit distinct geographic distributions compared to their climatological counterparts.

While climatological upper tropospheric and lower stratospheric (UTLS) PV intrusions are generally attributed to synoptic scale Rossby wave breaking, we find that SSW-related PV intrusions are governed by planetary scale wave disturbances that deform the extratropical meridional PV gradient maximum equatorward. As these deformations unfold, planetary-scale wave breaking along the edge of the polar vortex extends deeply into the subtropical and tropical UTLS. In addition, the material PV deformations also reorganize the geographic structure of the UTLS waveguide, which alters where synoptic scale waves break. In combination, these two intrusion mechanisms provide a robust explanation describing why displacement and split SSWs – or more generally, anomalous stratospheric planetary wave events – produce intrusions with unique geographic distributions: displacement SSWs have a single PV intrusion maximum over the Pacific Ocean, while split SSWs have intrusion maxima over the Pacific and Indian Oceans.

We also show that the two intrusion mechanisms involve distinct timescales of variability and highlight that they represent an instantaneous and direct link between the stratosphere and troposphere. This is in contrast to higher latitude stratosphere-troposphere coupling that occurs indirectly via wave-mean flow feedbacks.

1. Introduction

During Northern Hemisphere (NH) winter, the climatological time-mean zonal wind in the upper troposphere largely consists of westerly winds in the extratropics and easterly winds in the deep tropics (Webster and Holton 1982; Tomas and Webster 1994; Lee 1999). There are two notable exceptions to this pattern however, where westerly winds extend across the equator and connect the westerlies of the two hemispheres. These two regions – one over the eastern Pacific Ocean and another over the Atlantic Ocean – are generally referred to as 'westerly ducts' because linear Rossby wave theory predicts that waves with eastward absolute phase speeds that are less than the basic state zonal wind speed should be able to propagate through these ducts, thus dynamically linking the two hemispheres (Webster and Holton 1982; Kiladis and Weickmann 1992; Tomas and Webster 1994; Kiladis 1998; Waugh and Polvani 2000). The time-mean zonal wind pattern on the 350 K isentropic surface for boreal winter (DJF) is shown in Fig. 1a and the two westerly ducts are clearly visible in the Eastern Pacific and Atlantic Ocean basins along the equator.

At least in part due to refraction (Karoly and Hoskins 1982), Rossby waves emanating from the northern extratropics regularly propagate towards and sometimes into the core of the ducts, a situation that is graphically depicted by the arrows in Fig. 1a. The wave trains that propagate along these two pathways – often referred to as the South Eurasian/equatorial Pacific and North American/Atlantic waveguides (Hsu and Lin 1992) – form a well-known extratropical-tropical teleconnection pattern that are part of a subclass of planetary waveguides discussed in previous studies (e.g. Hoskins and Ambrizzi 1993).

As Rossby waves propagate along the Pacific and Atlantic waveguides, they eventually grow in amplitude and break (Scott and Cammas 2002; Abatzoglou and Magnusdottir 2006; Hitchman and Huesmann 2007). As the waves break, large intrusions of high PV air extend equatorward and downward from the lower stratosphere into the upper troposphere, while low PV tropospheric air concurrently extends upwards and poleward into the lower stratosphere (Riehl 1954; Murakami and Unninayar 1977; Frederiksen and Webster 1988; Appenzeller et al. 1996). While this type of wave breaking peaks in JJA (Postel and Hitchman 1999a), the strongest events that extend most deeply into the tropical upper troposphere occur predominantly in DJF (Waugh and Polvani 2000).

Interestingly, despite the tendency for wintertime Rossby waves to break almost exclusively over the Pacific and Atlantic basins, Nath et al. (2013) identified a strong PV intrusion over Gadanki, India in January 2009. Such a strong intrusion over the Indian Ocean sector is a interesting finding given the constraints imparted by local wave propagation conditions over southern Asia. Specifically, the strength of the meridional PV gradient along the southern flank of the Eurasian jet (Fig. 1a) normally endows the region with a strong enough waveguide as to retard the occurrence of Rossby wave breaking. This prompts two questions: (1) what could cause a large enough disturbance to the Eurasian jet and its associated waveguide that would permit the amplification and southward propagation of Rossby wave energy deep into the tropical upper troposphere over southern India; and (2) was the intrusion identified by Nath et al. (2013) a random event or might it be emblematic of a more general, but currently unidentified, region of intrusion activity? As we will show, answering both of these questions hinges on the presence and geographic location of the planetary wave structures associated with sudden stratospheric warmings (SSWs).

During the winter season, the NH stratosphere is characterized by the high PV air of the polar vortex, which is surrounded by the much lower PV air of the extratropical stratospheric surf-zone (McIntyre and Palmer 1983; Nash et al. 1996; Waugh and Polvani 2010). During undisturbed winters, the boundary between the surf-zone and the polar vortex is located near 60°N. However, during winters when a SSW occurs, the polar vortex, and hence the PV distribution of the stratosphere, are greatly disturbed in a geographically systematic fashion (Schoeberl 1978; Matthewman et al. 2009).

During a split SSW the stratospheric polar vortex (normally centered over the pole), is split into two daughter vortices with one vortex moving southward over Canada and the other vortex moving southward over Siberia. In contrast, during a displacement SSW the vortex remains largely intact, but it is displaced southward roughly over the North Atlantic/European sector. Despite their differences, both types of SSWs involve hemispheric-scale, coherent PV disturbances that deform the lower stratosphere's PV as far south as the northern subtropics. We propose that these PV deformations are associated with two separate wave processes that collectively explain why the largest PV intrusions in the upper troposphere and lower stratosphere (UTLS) occur during Northern winter.

In particular, our results will show that when a SSW occurs, the effects of planetary scale wave breaking that are normally confined to the extratropical stratosphere extend significantly equatorward in a zonally asymmetric fashion. As these equatorward surf-zone deformations unfold, vertically deep, hemispheric scale tongues of PV transect the UTLS and dynamically link the polar lower stratosphere to the tropical upper troposphere. In addition, the material PV deformations also modulate the synoptic scale waveguide structure in the subtropical and tropical UTLS. Indeed a hint of the modulation of the UTLS waveguide structure can be identified by comparing the climatological wind with the wind prior to the 2009 split SSW (Fig. 1).

Between January 16-22, 2009 (about one week prior to the central warming date), the westerlies in the Pacific duct are roughly twice as strong as the climatological westerlies (cf. Fig. 1a and b), which provides a more favorable background state for Rossby wave propagation deep into the tropics. Also, in contrast to the easterlies that are present throughout the tropical Indian Ocean in the climatology, the 2009 SSW period has a large region of westerly wind extending from southern India to the extratropical westerlies of the SH, which endows the tropics with a separate, geographically distinct westerly duct that links the Northern and Southern hemispheres.

Thus while previous studies have attributed the strongest DJF PV intrusions to synoptic scale wave breaking in the Pacific and Atlantic ducts, the 2009 SSW instead raises the possibility that it is the gravest scale planetary waves that provide the ultimate organizing force behind the largest PV intrusions during DJF. If this is true, then SSWs may represent an important and geographically distinct pathway for extratropical-tropical stratosphere-troposphere communication.

Several recent studies have examined the connection between SSWs, tropical convection (Kodera 2006; Kuroda 2008; Kodera et al. 2011; Sridharan and Sathishkumar 2011; Yoshida and Yamazaki 2011; Resmi et al. 2013), and gravity wave generation (Sathishkumar and Sridharan 2011; Nath et al. 2013). While these studies provide important evidence linking SSWs to the UTLS, they do not provide a systematic dynamical view that identifies how PV intrusions, barotropic wave trains, and the tropical circulation evolve during the life cycle of each type of SSW. For example, Martineau and Son (2013) note that there is a significant increase in meridional wave fluxes in the UTLS in the time period surrounding a SSW, but are unable to account for the increase using zonal-mean diagnostics (see also Limpasuvan et al. 2004). Nevertheless, Martineau and Son speculate that zonally asymmetric changes in stratospheric PV may help explain their finding.

To address the uncertain connection between SSWs, PV, and zonally asymmetric tropical UTLS variability, we detail how displacement and split SSWs are part of distinctly different patterns of climate variability that dynamically link the NH extratropical UTLS to the tropics of both hemispheres. In particular, we investigate how each type of SSW determines the geography of PV intrusions and the extratropical-tropical waveguide structure. Given these results, we discuss the implications that SSW-linked PV intrusions have for convection and the mixing of trace constituents in specific geographic regions of the tropical UTLS.

2. Data and PV Intrusion Identification

We use 6-hourly dynamical variables calculated from the ERA-Interim reanalysis data set (European Centre for Medium-Range Weather Forecasts 2009; Dee et al. 2011). Outgoing longwave radiation calculations use NOAA satellite twice daily data on a 2.5° grid (Liebmann and Smith 1996). All of the SSW 'central warming' dates are determined via the WMO criteria (McInturff 1978). Split and displacement SSW dates are listed in Table 1[1] of Albers and Birner (2014), with the exception that we include the 22 February 1979 split SSW. The split versus displacement determination is taken from Charlton and Polvani (2007) for the years 1979-2002; for the years 2003-2012, we determine split versus displacement SSWs based on Manney et al. (2009), Thurairajah et al. (2010), and Kuttippurath and Nikulin (2012).

We identify PV intrusions using an object-oriented algorithm that identifies contiguous regions of elevated PV via a magnitude-longitude-time criterion (see Appendix A of Dias et al. 2012 for details). The algorithm scans around a single latitude circle – chosen as 15°N in our analysis – on the 350 K isentropic surface and identifies any unique contiguous regions of elevated PV, where regions are contiguous in that they enclose a longitude-time 'area'. For example, Fig. 2a shows a longitude-time plot of PV for February 1999 with a horizontal black line on February 18 crossing through three contiguous regions of elevated PV near 60°, 240°, and 350° longitude. These three regions of PV enclose the tongues of PV shown in 2b as they extend equatorward across 15° N latitude and are advected eastward by the background flow. In our analysis, PV intrusions must meet all three of the following criteria: (1) the area inside the PV region must span at least 10° in longitude for the duration of the event; (2) the PV region must last at least one day; and (3) the entire longitude-time PV region must exceed 3.75 PVU (1 PVU = 10^{-6} K m^2 kg^{-1} s^{-1}). In general this leads to the identification of PV intrusion events that are 10°-40° in width and last 1-15 days in duration.

3. PV intrusion climatology

We begin by briefly describing the seasonality and basic features of strong PV intrusion events between 1979-2012. This serves the dual purpose of verifying that our intrusion

[1]The correct central warming date for the displacement SSW in 1984 is February 24.

identification algorithm is robust, while also providing a basis for comparing climatological PV intrusions with those that occur during SSW time periods.

Figures 3 shows the longitude-time distribution of PV (grey shading) at 15°N on the 350 K isentropic surface from 1979-2012. The figures also show the PV intrusions that are detected by our object identification algorithm where the centroid (in longitude-time) of each intrusion is depicted by a red '+' symbol. Because Fig. 3 shows 34 years of data, it is nearly impossible to see the fine scale structure of any of the individual PV intrusion events; thus to get a detailed view of what the intrusions look like we consider a longitude-time plot for single intrusion event later in this section. However, despite the lack of fine scale detail, several broad, yet important features are readily apparent only when viewing all 34 years in unison.

First, nearly all of the strong PV intrusion events occur in DJF. Second, there is a strong tendency for PV intrusions to occur at the longitudes of the Pacific and Atlantic westerly ducts, with the Pacific duct dominating the event count. And third, there appears to be a tendency for high intrusion activity to occur during winters with SSWs. This last point is particularly clear when the SSW-intrusion variability of the three decades are compared. Specifically, the 1979-1989 and 2000-2012 time periods are characterized by a relatively even distribution of SSWs and PV intrusions, while the 1990-1999 time period has almost no SSWs or PV intrusions except during the 1998/1999 winter season. In fact, 19 of the 22 years with a SSW between 1979-2012 are accompanied by high PV intrusion activity. Nevertheless there are some exceptions to the rule that strong PV intrusions and SSWs co-occur, but even the exceptional years do not necessarily represent counterexamples. For example, while no official SSW occurred during the winter of 2012, there was a minor SSW during mid-January which is coincident with high intrusion activity. This is perhaps not a surprising result in light of the fact that weak vortex events often barely miss achieving the major SSW criterion (Butler et al. 2014).

The seasonal and geographic distribution of the PV intrusion events that our algorithm identifies between 1979-2012 is qualitatively consistent with the 1980-1999 PV intrusion climatology of Waugh and Polvani (2000), except that our algorithm detects fewer, but stronger events, which is at least in part due to the fact that we chose a more stringent PV threshold criterion (Waugh and Polvani 2000 use 2 PVU at 10°N and group events together if they occur within 10° longitude and 6 days). While our algorithm identifies the Pacific and Atlantic ducts as the regions of strongest PV intrusion occurrence, if we look more closely at time periods immediately surrounding SSW central dates, a different duct structure begins to emerge.

Figure 2a shows a longitude-time plot of PV on the 350 K isentrope along 15° N latitude for 10-28 February 1999 for two PV thresholds. The red contour depicts the 3.75 PVU threshold used in our study. This threshold was chosen to be slightly higher than the 3.5 PVU threshold often used as a tropopause definition (Hoerling et al. 1991; Gettelman et al. 2011) because this way any contiguous region $\geq$3.75 PVU detected by our algorithm along the 350 K isentrope and equatorward of the subtropical jet likely represents stratospheric air being folded into the tropical upper troposphere. We also show the boundary for the 3.15 PVU threshold because this level most closely reproduces the results of Waugh and Polvani (2000); clearly our threshold captures a subset of the 3.15 PVU intrusions. In contrast to showing dual intrusion centers action over the Pacific and Atlantic ducts as occurs in climatology (Waugh and Polvani 2000), Fig. 2a shows primary centers of action over the Pacific and Indian Ocean basins. Figure 2b gives a more detailed view of the wave breaking occurring over the Pacific and Indian Ocean basins in the weeks before the central warming date (we discuss the wave breaking enclosed by the red 3.75 PVU contour in Section 5). While the $\sim$ 1-2.25 PVU intrusions that occur over the Indian Ocean are not identified by our algorithm, they are notably larger and significantly different than the DJF climatological PV distribution of $\sim$0.25 PVU (not shown) over the Indian Ocean at 15°N.

While our algorithm detects the strongest intrusions, Fig. 2a shows that the algorithm may not identify all of the intrusions that characterize the time periods immediately surrounding the occurrence of SSWs. To address this fact, our analysis in the following section compares composites based on the 3.75 PVU threshold with composites based on the weeks immediately prior to the central warming date. One minor limitation to comparing PV intrusions in this way is that neither method of identifying intrusions is able to discriminate between high PV air in the tropics that owes its presence to irreversible folding of PV filaments into the tropical upper troposphere versus reversible PV deformations that simply bulge the dynamical tropopause equatorward (c.f. Fig. 2 in Scott and Cammas 2002). However, our case study analysis later in the manuscript reveals that the PV anomalies we identify in our composites are in general associated with the stripping of filaments of high PV air off of the polar vortex and their advection equatorward. While we do not explicitly confirm that these filaments are part of irreversible mixing processes, most of the PV anomalies occur in association with reversals of the meridional PV gradient, which is suggestive of Rossby wave breaking and irreversible mixing (Hitchman and Huesmann 2007). Thus for the remainder of the paper we plot nearly all variables on the 350 K isentropic surface because it cleanly transects the UTLS in the latitudinal plane (cf. Gettelman et al. 2011 Fig. 2) and therefore provides a natural surface for interpreting PV disturbances that are likely to be associated with cross-tropopause mixing.

4. PV intrusion climatology during SSWs

In the previous section we observed that strong PV intrusions and SSWs tend to occur in tandem. We now explore whether the strength and location of PV intrusions differ significantly in the time period immediately surrounding the occurrence of a SSW and if so, whether those differences are unique for each type of SSW.

a. *Composite PV structure*

One major hypothesis of this manuscript is that the crucial ingredient for producing the largest PV intrusions is a planetary scale wave that is vertically deep enough that it retains a large amplitude nearly all the way downwards to the tropopause. As we will show, such a planetary wave structure can occur with or without the technical requirements for the occurrence of a SSW being met (Section 4c). Thus the only assumption implicit in our choice of the time averaging window used when building our SSW PV intrusion composites (defined below) is that the weeks surrounding a SSW will be, on average, characterized by strong and deep planetary waves (c.f. Fig. 10 of Albers and Birner 2014).

Figure 4a shows the composite PV anomaly from climatology for all of the Pacific intrusions identified in Fig. 3. Our climatology was generated by averaging the full 34-year data set into a single 365-day time series and then retaining only the first three harmonics. The anomaly was then calculated by subtracting the PV climatology from the full PV field for each of the days that our PV intrusion threshold conditions were met (Section 2), and then time averaging the resulting data. In essence Fig. 4a depicts a 'smeared' out view of all of the wave breaking events that are denoted by the red '+' symbols in Fig. 3. The predominant feature is the dipole structure in the Pacific duct that is indicative of wave breaking that systematically exchanges high PV air equatorward and low PV air poleward. In composite, the magnitude of the Pacific duct intrusion maximum is $\sim 1.5 \times 10^{-1}$ PVU between 10°-20°N.

To compare our 3.75 PVU threshold intrusion composite with the intrusions that occur surrounding SSWs time periods, we produced PV anomaly composites for three different SSW categories: one for all SSWs, one for split SSWs, and one for displacement SSWs. The anomalies in the composites are produced by subtracting the seasonally specific days in the PV climatology from the full PV field on the 350 K isentrope for the two weeks before and two weeks after the central warming date and then time averaging the resulting data.

Three features stand out in the composite for all SSWs (Fig. 4b). First, while the 3.75

PVU threshold composite is dominated by a single PV anomaly dipole in the Pacific duct, the SSW composite has two sets of PV anomalies: one over the Pacific duct, and a second near 50° E. Second, the pair of PV anomalies over the NH Pacific and Indian Ocean basins have hemispherically symmetric anomaly pairs across the equator in the SH. And third, the magnitude of the PV anomalies maximize at 3.15 $\times 10^{-1}$ PVU and -1.4 $\times 10^{-1}$ PVU between 10°-20° N and S, respectively, in the Pacific duct and 2 $\times 10^{-1}$ PVU and -1.2 $\times 10^{-1}$ PVU between 10°-20° N and S, respectively, in the central Indian Ocean (hereafter referred to as the Indian duct).

Thus in the two weeks before and after a SSW, PV intrusions are (in a composite sense) twice as strong as the 3.75 PVU threshold intrusions. In fact, the SSW PV anomalies are likely even stronger than they appear in Fig. 4b because as mentioned above, the data is averaged into the anomaly over the entire four week period surrounding each SSW regardless of whether our intrusion threshold criterion is met. It is also notable that while the PV anomaly pattern in Fig. 4b peaks around the central warming date, the pattern exists 40 days before and after the central warming date (not shown), though the anomalies are in general stronger prior to the central warming date.

While the dual PV anomaly pattern just described is based on the composite for all SSWs, it nevertheless reflects the dual westerly wind duct structure that occurred during the 2009 split SSW (Fig. 1b). This is no coincidence because the Indian Ocean PV feature can be accounted for by considering the composite PV anomaly pattern for split and displacement SSWs separately. Comparing Figs. 5a and b we see that nearly all of the PV anomaly signal that is centered over the Indian Ocean in Fig. 4b can be attributed to split SSWs. Indeed, the displacement anomaly over the Indian Ocean has a rather weak subtropical and tropical amplitude ($\sim 1 \times 10^{-1}$ PVU), while the split anomaly peaks at 3.4 $\times 10^{-1}$ PVU in the NH between 10°-20° N and -2.5 $\times 10^{-1}$ PVU between 10°-20° in the SH. The anomalies in the NH and SH portions of the Pacific duct are also slightly larger for split SSWs (4 and -2.5 $\times 10^{-1}$ PVU, respectively) when compared to displacement SSWs (3.4 and -1.8 $\times 10^{-1}$ PVU, respectively).

To help quantify the SSW PV anomalies we compare probability density functions (PDFs) for the SSW versus climatological time periods. The SSW PDF is generated using all 6-hourly data values at each geographic point on the 350 K isentrope in the two weeks prior to all 22 SSWs. The climatological PDF is generated using a bootstrap method. For example, if a SSW occurs in February, then we select a random two week period from any February in the 1979-2012 period subject to the constraint that if the randomly selected two week period occurs within 40 days of any of the 22 central warming dates, then that period is rejected and a new two week period is queried. We repeat this process until 100 two week periods are generated for each of the SSWs, and we then build a PDF based upon the resulting data.

Figure 6a shows the difference in the 90th percentile of PV between the SSW and random PDFs; the largest differences are collocated with the PV anomalies shown in Fig. 4b. The 90th percentile increase in PV peaks at ∼1 PVU over the Pacific and Indian duct regions; the difference in the 50th and 75th percentiles (not shown) peak in the same locations at 0.5 and 0.8 PVU, respectively. Figure 6b compares the SSW (blue line) and random date (red line) PDFs for the region of the Pacific duct outlined by the black box in Fig. 6a, where the dotted red lines surrounding the random date PDF curve denote the boundaries of the 95% bootstrap confidence interval. What this shows is that the wave breaking increases the variance of PV, which is reflected in the higher frequency of low and high PV and lower frequency of PV near the 50^{th} percentile of the climatological distribution (∼0.25-0.5 PVU). However, because there is a preference for equatorward wave breaking (anticyclonic) in our case, there is a corresponding preference for the introduction of high PV air into the region enclosed by the box in Fig. 6a. The bulk of the increase in PV shown in our anomalies is due to an increased occurrence of wave breaking events that introduce 3-7 PVU magnitude air into the subtropical UTLS.

One difficulty with interpreting Figs. 6a and b is that similarly to Fig. 4b, they depict a spatial-temporal average and thus each spatial point in the composites is made up of a selection of time periods with and without wave breaking occurring. To try and mitigate this effect, we also calculated a spatial-temporal average using a smaller space-time window (see the Figure caption for details). The result of this calculation is shown as a box plot in Fig. 6c, which shows that the median for the SSW time period is near to the boundary of the 75th percentile of the distribution for the randomly selected dates, while the mean of the SSW periods lies well outside the 75th percentile of the random dates. In combination, Figs. 6a-c show that broad regions of the Pacific and Indian ducts experience a statistically significant increase in the mean and tails of their PV distributions during the weeks preceding a SSW.

5. Analysis of PV intrusion mechanisms

The large PV intrusions that are the subject of this study are traditionally thought to arise from synoptic scale waves that propagate and occasionally break along the waveguides of the UTLS. However, the central hypothesis of this manuscript is that the largest PV intrusions arise due to – or in conjunction with – planetary waves that attain their largest amplitudes in the interior of the stratosphere. If this hypothesis is correct, then the largest PV intrusions should have planetary wave signatures that remain coherent between the interior of the stratosphere and the tropopause. We test this premise in Section 5a.

In addition, we contend that SSW-related PV intrusions exhibit three key dynamical features: (1) amplified anticyclones – one for displacement SSWs or two for split SSWs – that are associated with low-frequency planetary wave surf-zone dynamics; (2) modifications to the synoptic waveguide structure; and (3) positive (southwest to northeast) tilt of the low-frequency planetary wave stream function pattern. All three of these features are related because they owe their existence to the shape of the material PV deformations imparted by the planetary wavenumber of the SSW. The relative importance of synoptic versus low-frequency variability for producing these features is examined in detail in Sections 5b and 5c.

a. Vertical coherence of PV structures

Detailed analysis of the 1999 and 2009 split SSWs have been carried out by several studies (Charlton et al. 2004; Albers and Birner 2014 and references therein). Both SSWs were characterized by vertically deep, nearly barotropic planetary wavenumber two patterns with low pressure centers located over Asia and North America, which is consistent with both observational (Matthewman et al. 2009) and modeling (Esler and Scott 2005; Matthewman and Esler 2011) analyses of split SSWs. For example, Fig. 7 shows PV on various isentropic surfaces on 14 and 20 January 2009. A planetary wavenumber two structure exists over a deep layer of the atmosphere and the signature of planetary wave breaking within the stratospheric surf-zone (McIntyre 1982; McIntyre and Palmer 1983) is apparent on the 700 K isentrope.

Although the two dominant regions of wave breaking at all heights are collocated with the two amplifying anticyclones near 40° and 250° longitude, it is not clear whether the wave breaking and filamentation in the interior of the stratosphere is related to the intrusions occurring on the 350 K isentrope. Nevertheless, the wave breaking experiments of Polvani and Saravanan (2000) suggest that the tongues of PV associated with planetary wave breaking may remain coherent over as many as three scale heights before they become significantly stretched out and filamented (c.f. their Fig. 5); this alludes to the possibility that the largest PV filaments on the 350 K isentrope may actually be the lowermost manifestation of the large scale wave breaking occurring in the interior of the stratosphere.

To test this hypothesis, we compare the horizontal wave breaking structures between the 350 and 600 K isentropes with latitude-height cross sections of modified PV, which is defined as $\widetilde{\mathrm{PV}} = \mathrm{PV} * (\theta/\theta_0)^{\alpha}$ where θ is potential temperature and α is a scaling parameter. We use $\widetilde{\mathrm{PV}}$ because it aids with the visualization of PV isosurfaces across several scale heights (Lait 1994; Müller and Günther 2003), while leaving the conservation properties of PV unchanged. Different values for θ_0 and α can be chosen that highlight different regions of PV in the height plane; for our plots we used $\theta_0 = 350$ K and α =-4, which highlights isosurfaces that extend upwards from the 350 K isentrope.

Figure 8a shows $\widetilde{\mathrm{PV}}$ on the 350 K isentrope with the 600 K isentrope 8.5 $\widetilde{\mathrm{PVU}}$ isoline overlaid for 19 January 2009. The amplifying planetary wavenumber two that exists in the middle stratosphere on the 600 K isentrope has a clear imprint on the horizontal organization of PV on the 350 K isentrope. To test how vertically coherent the wave breaking is between these two levels, Figure 8b shows a cross-section of $\widetilde{\mathrm{PV}}$ averaged between 238°-240° longitude; the location of this cross-section is depicted in Figure 8a by the dashed black line. Figure 8b shows that the wave breaking occurring on the two isentropic surfaces are part of vertically coherent PV structures that span at least the 320 to 625 K isentropes. For example, comparison with the 1979-2012 DJF average $\widetilde{\mathrm{PV}}$ for the Pacific duct (Fig. 8c) reveals that on January 19 the 5 and 6.5 $\widetilde{\mathrm{PVU}}$ surfaces (blue and black dotted lines, respectively) have been perturbed upwards from 325 K to 500-635 K near 60° latitude, while those same $\widetilde{\mathrm{PVU}}$ levels have been perturbed downward from the 400-600 K levels to below 350 K near 35° latitude.

Note that it is important to exercise care when interpreting the $\widetilde{\mathrm{PV}}$ cross sections because despite the fact that the $\widetilde{\mathrm{PVU}}$ isolines in Fig. 8b appear to be curling directly in the latitude-height plane, this does not necessarily indicate vertical overturning. Rather the upward perturbed $\widetilde{\mathrm{PV}}$ isolines near 60° N in Fig. 8b highlight the poleward, anticyclonic curling of low PV along curve (A) in Fig. 8a, while the downward perturbed isolines near 35° N in Fig. 8b highlight the equatorward curling of high PV along curve (B) in Fig. 8a. A three-dimensional view of this type of wave breaking along the periphery of the polar vortex using a high resolution contour dynamics model is presented in Polvani and Saravanan (2000).

Figures 8d and e show an analogous situation to that just described, but for the February 1999 split SSW. The main difference between the two SSWs is that the 1999 event was not quite as deep and thus there is less vigorous anticyclonic overturning of PV along the 350 K isentrope in the eastern Pacific. As a consequence, the $\widetilde{\mathrm{PV}}$ isosurfaces are not perturbed as far upwards or downwards in the latitude-height plane (Fig. 8e). Because of the more shallow vertical scale of the wave breaking, the 530 K level 6.5 $\widetilde{\mathrm{PVU}}$ isoline is used as the upper level overlay on Fig. 8d. Nevertheless, there is still clear coherent organization of PV across multiple scale heights as the 6.5 $\widetilde{\mathrm{PVU}}$ isoline is perturbed upwards to 650 K, while the tongue of high PV air rotating clockwise and equatorward near 205° in Fig. 8d results in the tongue of 3-4 $\widetilde{\mathrm{PVU}}$ air wrapping downwards to the 350 K isentrope near 15° N in Fig. 8e and the 3 $\widetilde{\mathrm{PVU}}$ isoline extending nearly to the equator along the tropopause.

b. Synoptic- and low-frequency wave trains

Figures 9a,b show the low-frequency and synoptic stream functions for 14 January 2009 on the 350 K isentrope. In order to get a feel for how the synoptic and low-frequency variability corresponds to the active wave breaking on the same date, Figs. 9c-d show PV on the 350 K isentrope with select stream function isolines overlaid. The stream function isolines in Fig. 9c,d correspond to those shown in Fig. 9a-b, except that for the low-frequency variability we have extended the band-pass filter out to one year to retain the seasonal cycle because it provides a clearer picture of the total low-frequency planetary scale pattern.

Figures 9a,c clearly depict the strong anticyclone located over the central Pacific (240° longitude) and the amplifying anticyclone located over central Asia (30° longitude) that are together associated with the growing SSW-related planetary wavenumber two pattern (Fig. 7). Figures 9b,d on the other hand show that the equatorial Pacific waveguide is essentially devoid of any synoptic scale wave trains that might help explain the already deeply amplified PV intrusion located around 240°. This is in contrast to the obvious synoptic scale (∼wavenumber five) wave trains propagating along the corresponding SH extratropical waveguide near 45° S. Thus in combination, Figures 9a-d confirm that the twin anticyclones were the dominant dynamical feature during the 2009 SSW period. As these anticyclones amplified, their eastern flanks repeatedly stripped large filaments of high PV air off of the polar vortex and advected them equatorward. These filaments are part of the deep vertical PV structures identified in Fig. 8 and are representative of stratospheric surf-zone dynamics bulging strongly equatorward over the Indian and Pacific basins where it is likely that the filaments of PV are ultimately folded into the tropical upper troposphere.

In contrast, the 1999 SSW was governed by a more even mixture of the three dynamical features mentioned at the beginning of Section 5. Similar to the 2009 SSW, the amplifying low-frequency anticyclone in the eastern extratropical Pacific (Fig. 10a) is strongly contributing to the wave breaking observed on the 350 K isentrope (Fig. 10c). However, the 1999 SSW was also characterized by significant synoptic scale wave activity, which was modulated by both the shape of the material PV deformations and the tilt of the underlying low-frequency planetary wave.

In particular, because synoptic scale wave trains are guided along strong meridional PV gradients – and ultimately towards regions of higher total Rossby wavenumber (Hoskins and Karoly 1981; Hoskins and Ambrizzi 1993) – the amplifying planetary wave imparts a wavenumber two PV pattern to the synoptic scale waveguide structure that preferentially guides the waves into the Indian and Pacific ducts. The effects of the modified waveguide structure due to the planetary wavenumber two induced PV deformation is apparent in the pattern of synoptic scale wave trains highlighted by the dashed lines in Fig. 10b,d that connect the local maxima of the synoptic scale stream function pattern. It is this type of deformation that is responsible for the dual wind duct structure shown in Fig. 1b and the total Rossby wavenumber on the 350 K isentrope (discussed in more detail below).

In addition, the amplifying anticyclone center over the Pacific basin provides a low-frequency dipole stream function pattern with positive tilt (black dashed lines in Fig. 10a). While there is a amplifying anticyclone between 0°-50° longitude related to the growing planetary wavenumber two, it is not yet intense enough to impart a strong dipole pattern with positive tilt over the Indian basin. Similar positively tilted dipole patterns are apparent during the 2009 SSW over the Indian and Pacific basins (Fig. 9a). These low-frequency patterns provide a basic state that yields a constructive interference pattern when any positively tilted synoptic scale waves pass through. That is, as the synoptic waves shown in Fig.

10b propagate eastward and equatorward into the Indian and Pacific ducts, they positively contribute to the ongoing anticyclonic low-frequency wave breaking. Indeed the combined effect of the two time scales of variability on the overall wave breaking pattern is clear in when Figs. 10c and d are compared.

A similar pattern of co-variability between synoptic and low-frequencies also occurs during displacement SSWs, though the intrusions are largely confined to the Pacific basin. For example, most of January and all of February 2008 was characterized by a positively tilted low-frequency stream function dipole pattern (not shown) over the Pacific basin; this pattern eventually culminated in the displacement SSW on February 22. At its strongest, the low-frequency pattern stretched from 15°S to 90°N and was associated with a large and slowly evolving pattern of high PV air intruding deeply into the tropical Pacific basin. As this low-frequency pattern evolved over the roughly two month period, it was punctuated by occasional synoptic scale wave trains. In combination, the two scales of variability led to the high incidence rate of deep tropical intrusions during the 2008 winter season shown in Fig. 3c.

The relative contribution of synoptic versus low-frequency variability can be further examined via consideration of the dual Pacific and Indian duct waveguide pattern apparent in the total Rossby wavenumber on the 350 K isentrope. The total Rossby wavenumber for plane wave solutions to the barotropic vorticity equation on a sphere (Hoskins and Karoly 1981; Barnes and Hartmann 2011) is given by

$$K = \cos\theta\left(\frac{\beta^*}{\overline{u} - c}\right)^{1/2}, \tag{1}$$

where

$$\beta^* = \frac{2\Omega\cos\theta}{a} - \frac{1}{a^2}\frac{\partial}{\partial\theta}\left[\frac{1}{\cos\theta}\frac{\partial}{\partial\theta}(\overline{u}\cos\theta)\right], \tag{2}$$

is the meridional gradient of absolute vorticity; Ω is the Earth's rotation rate; θ is latitude; a is the radius of Earth; $\overline{u}$ is the background zonal wind speed; and c is the absolute zonal phase speed for transient waves. In Fig. 11 we plot the stationary total Rossby wavenumber

($c = 0$), where the filled contours highlight the regions that barotropic Rossby waves will tend to propagate towards (Karoly and Hoskins 1982; Hsu and Lin 1992; Hoskins and Ambrizzi 1993) and the dotted lines depict the corresponding critical lines. Choosing $c = 0$ for our phase speed is sufficient for gaining a qualitative picture of any wind duct structure, but we note that the strength, and therefore width, of any westerly duct is sensitive to the size of the background zonal wind and the phase speed of the synoptic scale waves.

The Indian and Pacific ducts are easily identified in the total stationary Rossby wavenumber squared for 18-24 February 1999 (Fig. 11a). The Pacific duct looks qualitatively similar to its climatological counterpart (not shown) because of the climatological westerly winds that occur in the tropical eastern Pacific (Fig. 1a). The Indian duct on the other hand appears strikingly different than climatology. Specifically, the climatological easterly winds that straddle the equator over the Indian basin (Fig. 1a) contribute to the formation of a critical line during DJF that extends along 10° N between 0°-180° longitude (not shown). In sharp contrast, the weeks prior to the 1999 SSW are characterized by a deep westerly duct that extends all the way to 10-15° S (a similar duct structure mirrors the winds structure shown in Fig. 1b during the 2009 SSW). Similar patterns occur for the other split SSWs in the record with two exceptions.

In order for synoptic scale waves to make a strong contribution to the Indian Ocean PV anomalies seen in Figs. 5 and 6, a westerly wind duct must extend deeply into the tropics over a reasonably wide longitudinal scale, and the duct must persist for long enough for the waves to propagate sufficiently equatorward. For example, while there was a strong planetary wavenumber two PV deformation associated with the February 1989 split SSW, its Eurasian low-pressure center did not impinge far enough equatorward to form a significant synoptic scale waveguide deep into the tropics. Likewise the well-studied 1979 split SSW formed a relatively weak Indian duct. As result, the Indian basin PV anomalies during these two SSW periods were due almost solely due to low-frequency wave breaking. However, when the total Rossby wavenumber is composited over the week period prior to the remaining split

SSWs in the record, there is a very obvious Indian westerly duct that extends cleanly into the Southern Hemisphere (Fig. 11b). For the Indian ducts documented here, the westerly winds appear to be most closely associated with the wind field endowed by the planetary wave PV deformations, though the role of equatorial Rossby waves and Walker-like mass circulations associated with convection over Africa may play a role (see Section 5d).

c. *February 2010 and January 2012*

We now try to understand why some SSWs are not accompanied by high intrusion activity, while other time periods with high intrusion activity do not appear to be associated with SSWs. In contrast to the 2009 SSW (Fig. 7), the February 2010 SSW exhibited virtually no planetary wave signature along the 350 K isentrope to correspond with the SSW-related PV disturbance in the middle stratosphere (not shown) in the week prior to the 10 February central warming date. Indeed the low-frequency stream function (Fig. 12a) is essentially a weak analogue of the seasonal stream function pattern and thus there is no discernible SSW-related planetary wave signature in the PV distribution on the 350 K isentrope (Fig. 12c). Consequently virtually all of the PV disturbances along the 350 K isentrope during this time period were due to synoptic scale waves near 30°N (Fig. 12b,d). As a result, the PV intrusions associated with the wave breaking on the 350 K isentrope are rather weak in latitudinal scale (∼25° in width) and are confined to the region poleward of 15°N.

In contrast to February 2010, January 2012 had a substantial amount of intrusion activity (Fig. 3c) but no official SSW as defined by the WMO definition (McInturff 1978). Nevertheless, there was a substantial wavenumber one minor stratospheric warming that was caused by a planetary wave disturbance that extended from the 350 K isentrope into the interior of the stratosphere (not shown). Similar to the 2010 case, there is evidence to suggest that synoptic scale wave breaking (Fig. 13b,d) played a role in the PV exchange along 350 K isentrope. However, unlike the 2010 time period, the planetary wave perturbation seen in the middle stratosphere extended downwards to at least the tropopause, which manifested itself as the major low-frequency anticyclone centered around 175° (Fig. 13a). Indeed the imprint of the low-frequency variability on the Pacific intrusion activity can be confirmed by noting that the total low-frequency stream function zero level isoline very closely matches the PV deformation on the 350 K isentrope (Fig. 13c), and that the stream function pattern has positive (southwest to northeast) tilt (Fig. 13a) that, in combination with the synoptic scale wave activity (Figs. 13b,d), yields a constructive interference pattern. These results highlight that it is the deep vertical scale of the planetary wave – rather than the technical requirements of major SSW being met – that is the crucial ingredient for producing the largest intrusions.

d. Connection to the Madden-Julian Oscillation

The current manuscript is principally focused on explaining why SSW-related intrusion activity is governed by the wavenumber of intraseasonal and synoptic scale planetary wave perturbations, and thus we have not addressed the fact that our results rely in part on filtered data that overlaps in frequency space with the Madden-Julian Oscillation (MJO). However, this may prove to be an important avenue of exploration because it is possible that the MJO implicitly modulates the strength of PV intrusions via both the initiation of the SSW planetary waves themselves (Garfinkel et al. 2012; Liu et al. 2014) as well as via changes in the large scale tropical and subtropical flow patterns that control the equatorial Pacific waveguide (e.g. Walker-type mass circulations and equatorial Rossby gyres). In light of this relationship, we briefly discuss possible connections between our results and prior MJO-SSW related work.

Garfinkel et al. (2012) and Liu et al. (2014) offer conflicting conclusions on the nature of the relative connection between the MJO and split versus displacement SSWs. In particular, Garfinkel et al. (2012) found no difference in the role of the MJO based on SSW type and propose that in the two week period prior to both types of SSWs, the real-time multivariate (RMM) MJO index (Wheeler and Hendon 2004) is primarily in phases 7 and 8. In contrast, Liu et al. (2014) found that RMM phase 7 and 8 type variability is associated with split SSWs but not displacements. Based on outgoing longwave radiation (OLR) during these two phases[2], convection is suppressed over the Maritime Continent and enhanced over the central Pacific basin, and there are associated stream function dipole patterns in the upper troposphere that impart anomalous easterly winds along the equator between $\sim$150°-220°E (i.e., 150°E - 140°W) and anomalous westerly winds along the equator beginning at $\sim$230°E (130°W) and extending eastward all the way to $\sim$140°E (140°E). Thus during these two phases of the MJO, the wind field will act to enhance any nascent westerly duct structures over the far eastern Pacific and Indian Ocean regions.

Figures 14a and b show 20-120 day filtered OLR composited over the two weeks prior to all split and displacement SSWs, respectively, where anomalies are only plotted if they are significantly different from the 1979-2012 DJF climatology at the 95% confidence level using a two-tailed Student's t-test. The split SSW negative OLR anomaly over central Africa, the positive OLR anomaly over the Maritime continent, and the minor negative OLR anomaly just south of the equator centered at 180° is consistent with the composite phase 1, 7, and 8 RMM pattern discussed above, while the negative OLR anomaly over the Maritime continent for displacement SSWs is more consistent with RMM phases 4-6. This result offers some support to the suggestion by Liu et al. (2014) that MJO phase 7 and 8 type variability is more strongly associated with split SSWs and lends some provisional support to the notion that MJO-like variability may contribute to sustaining the dual westerly duct structures that occur during split SSWs. At present it is unclear whether the OLR anomalies – and any associated convection – are triggers for or results of the PV intrusions documented earlier in the manuscript. For example, it is plausible that the strong negative OLR anomaly over central Africa (Fig. 14a) may have helped excite a combination of equatorial Rossby wave

[2]The upper tropospheric circulation features and OLR anomalies associated with each phase of the RMM index can be viewed on the National Oceanic and Atmospheric Administration MJO Indices website at: www.esrl.noaa.gov/psd/mjo/mjoindex/

and divergent mass circulations (e.g. Sardeshmukh and Hoskins 1988) over the Indian ocean basin that helped sustain the westerly wind ducts discussed in Section 5b.

MJO-like OLR signals are not the only interesting feature observed in our OLR anomalies. For example, the systematic geographic locations of the planetary wave disturbances associated with displacement and split SSWs is evident in the NH polar regions where a clear wavenumber one and two OLR pattern is observed (Figs. 14b and a, respectively). The dominant pattern in this case is the clear tendency for positive OLR anomalies to be collocated with the stratospheric cyclonic features over Asia and N. America (splits) and N. America only (displacements). In addition, the regions of strongest elevated PV near the equator for split SSWs ($\sim$240° in Fig. 5a) and displacement SSWs ($\sim$210° in Fig. 5b) are collocated with positively titled negative OLR anomalies, which is to be expected from previous work connecting OLR and PV intrusions (Kiladis 1998; Waugh and Funatsu 2003). In summary, there is intriguing evidence that the MJO may act in concert with the large scale circulation to favor regimes that are conducive to SSW-related PV intrusions, but more work is necessary to further quantify such a relationship.

6. Conclusions

During Northern winter, Rossby waves are readily observed propagating eastward along the South Eurasian and North American waveguides and then equatorward into the Pacific and Atlantic westerly ducts (Fig. 1a). Perhaps not surprisingly, most studies examining the dynamics of NH DJF extratropical-tropical PV intrusions have focused on the role of synoptic scale variability (e.g. Webster and Holton 1982; Kiladis and Weickmann 1992; Hoskins and Ambrizzi 1993; Kiladis 1998; Waugh and Polvani 2000). Under this paradigm, nearly all of the subtropical cross-tropopause mixing associated with PV intrusions is accomplished by breaking synoptic scale Rossby waves – a situation graphically depicted by the blue arrows in Fig. 15a – and it is generally assumed that the large-scale atmospheric mixing due to planetary waves breaking in the surf-zone is wholly contained in the stratosphere – shown as the red arrows in Fig. 15a.

In contrast, we propose that there is a class of significant PV intrusions resulting from the dynamics of planetary wavenumber one and two perturbations (e.g. SSWs) that deform the extratropical meridional PV gradient significantly equatorward. The effects of such PV deformations manifest themselves in two important ways, which we summarize below for a wavenumber two (split) SSW:

1) As the amplitude of a planetary wave within the stratosphere grows, the two low-pressure centers of the polar vortex move equatorward; this is illustrated by the green arrows in Figs. 15b,c. As this process unfolds, the planetary breaking in the surf-zone (McIntyre and Palmer 1983) that was once contained entirely in the stratosphere begins to impinge upon the subtropical tropopause and tropical upper troposphere. The impingement of stratospheric wave breaking on the tropopause – depicted by the red arrows in Fig. 15c – primarily occurs upstream of the troughs along the longitudes (black dashed lines in Fig. 15b) where the anticyclones repeatedly shear off filaments of high PV air from the lobes of the polar vortex and advect the filaments equatorward. Under extreme circumstances (e.g. the 2009 SSW), this type of large-scale wave breaking overwhelms the effects of synoptic scale waves and provides the dominant background configuration for anomalous PV intrusions. Nevertheless, the underlying PV deformation also interacts with synoptic scale waves, which in turn contributes to intrusion activity (described next).

2) The planetary scale PV deformations (green lines in Fig. 15b) also cause significant changes to the synoptic scale waveguide (e.g. Fig. 11); the result is the preferential ducting of synoptic scale wave activity into the Pacific and Indian ducts along the blue arrows in Fig. 15b where the PV anomalies surrounding SSW time periods are strongest (Fig. 4b).

In combination, the synoptic and low-frequency variability that underlies these two mechanisms imparts the Pacific and Indian duct regions with positively tilted (southwest to northeast) stream function patterns (Figs. 9, 10, and 13). This tilt orientation implies equatorward energy propagation (Starr 1948; Hoskins and Karoly 1981) with the low-frequency pattern providing a basic state onto which any positively tilted synoptic scale wave disturbances can project onto as they propagate into the westerly ducts. Thus in a linear sense, the two scales of variability yield a constructive interference wave pattern that should lead to strong combined equatorward energy flux. In a nonlinear context, mutual reinforcement of the low-frequency and synoptic scale variability may also occur via direct interactions between the two wave scales (Cai and van den Dool 1991; Branstator 1995; Jin et al. 2006 and references therein), but assessing this possibility remains untested by the current work.

Regardless of the relative mixture, these physical mechanisms form a dynamical framework that explains why the largest NH PV intrusions occur in a geographically systematic fashion that is dependent on whether a split or displacement SSW – or more generally whether a planetary wavenumber one or two disturbance – is triggering the response. Specifically, displacement SSWs are characterized by a single PV intrusion maximum that is collocated with the climatological PV intrusion maximum in the tropical eastern Pacific basin. Likewise split SSWs also have a PV intrusion maximum in the eastern Pacific basin, but additionally have a secondary intrusion maximum over the tropical Indian Ocean. This geographic pattern provides a UTLS manifestation of the finding by Matthewman et al. (2009) that the locations of the vortex core(s) during displacement and split SSWs have systematic geographic preference.

In addition to explaining the geographic location of our PV intrusion composites, the vertical structure of split versus displacement SSWs also helps to explain the relative strength of our intrusion composites. In particular, our results suggest that when planetary wave disruptions are vertically deep – regardless of whether an official SSW occurred – then the underlying planetary scale PV structure will initiate vertically deep intrusion structures that can span from the polar regions to the tropics in longitudinally localized regions of the Northern Hemisphere (e.g. during January 2009). However when large scale planetary wave disruptions are confined to the interior of the stratosphere (e.g. during February 2010), then PV intrusions will be much smaller in latitudinal scale and will be more reflective of more common synoptic scale Rossby wave breaking (Postel and Hitchman 1999b). Indeed this result helps to explain why deep intrusion activity is generally weaker for displacement SSWs than for split SSWs (Fig. 5). That is, the barotropic vertical structure of split SSWs (Matthewman and Esler 2011) makes them much more likely to have planetary wave structures that extend to at least the tropopause versus the first baroclinic vertical structure of displacement SSWs (Esler and Matthewman 2011) where the planetary wave perturbation is maximized in the upper stratosphere and decays with decreasing height.

While our results characterize the co-evolution of vertically deep planetary waves and associated PV intrusions, our analysis makes no assumption regarding the direction of causality between PV intrusions and SSWs. For example, if SSWs are caused by anomalous forcing from the troposphere, then the intrusions documented in this study may be the signature of tropopause level precursor events. In contrast, if SSWs are triggered by internal stratospheric variability (e.g. Scott and Polvani 2006; Esler and Matthewman 2011; Matthewman and Esler 2011; Albers and Birner 2014), then the intrusions may simply be a relatively passive by-product of the amplifying planetary waves themselves. Regardless of how the planetary waves that are at the core of this study arise, the deep vertical scale of the associated material PV deformations and intrusions have implications for the interpretation of stratosphere-troposphere coupling during time periods when the polar vortex is strongly disturbed.

In particular, the potential for strong cross tropopause mixing of PV during the intrusion events documented in this study represents a direct and near instantaneous coupling between the dynamics of the upper troposphere and the interior of the stratosphere. This is in contrast to annular mode and Arctic oscillation variability (Thompson and Wallace 1998;

Baldwin and Dunkerton 1999; Thompson and Wallace 2000; Baldwin and Dunkerton 2001) where the effect of stratospheric wave flux anomalies are communicated to the troposphere indirectly via wave-mean flow feedbacks. Still, because the wave fluxes that are responsible for the downward propagating zonal mean wind anomalies are also at least partly responsible for the material PV deformations and large-scale wave breaking that govern the PV intrusions, these two mechanisms for coupling the stratosphere-troposphere system cannot be completely interpreted in isolation. Indeed anomalous vortex events are by definition highly nonzonal in character, a fact which is implicit in studies that have connected stratospheric vortex variability to surface temperature anomalies via modulations of synoptic scale wave patterns (Charlton et al. 2004) and PV intrusion events (Cai 2003). However, at present it is unclear if there is any direct relationship between the longitudinally dependent nature of the tropospheric weather patterns identified by Thompson and Wallace (2001) and the PV deformations and intrusions documented in the current manuscript. Nevertheless, our results provide one potential dynamical framework – outlined as items (1) and (2) above – through which to understand how and why scale interactions between synoptic scale and planetary low-frequency variability combine to produce episodes of anomalous weather and climate in specific geographic localities during periods when the polar vortex is strongly disturbed.

Our results also raise additional questions regarding the connection between SSW-related PV intrusions and tropical-extratropical convection (Kiladis and Weickmann 1992; Kiladis 1998; Funatsu and Waugh 2008) and constituent transport (Appenzeller et al. 1996; Scott et al. 2001; Waugh and Funatsu 2003; Leblanc et al. 2004; Hsu et al. 2005; Waugh 2005; Sherwood et al. 2010; Tsidu and Ture 2013). For example, the strong geographic localization of intrusions during split versus displacement SSWs may modulate whether anomalous tropical convection or extratropical-tropical water vapor exchange will occur over one or both of the Pacific and Indian Ocean basins (Fig. 14). Likewise, localized ozone intrusions during SSWs may be of importance for air quality given that Cooper et al. (2005) and Langford et al. (2014) have provided evidence that PV intrusions may be responsible for supplying ozone all the way to the surface of the Earth, which may directly affect air quality in the Earth's boundary layer.

The distinct geography of the intrusions may also be important in terms of the tropical tropopause layer. For example, Munchak and Pan (2014) recently suggested that wave breaking in westerly ducts has a significant effect on the location and seasonality of the separation between the cold point and lapse rate tropopause heights, which in turn has implications for exchange processes between the tropical tropopause layer and the extratropical lowermost stratosphere (Gettelman et al. 2011; Randel and Jensen 2013). Moreover, Kim et al. (2015) observed that the seasonal cycle of UTLS tropical upwelling has a planetary wavenumber three pattern with centers of action at 60°, 230°, and 300° longitude; whether these centers of action are related to the wave breaking in the Indian, Pacific, and Atlantic westerly ducts examined in this manuscript remains an open question.

Finally, there is one important feature of the SSW PV anomalies that we have not discussed. That is, the anomaly patterns shown in Fig. 5 are hemispherically symmetric (i.e. have mirror images across the equator). One possible reason for this symmetry is that the material PV deformations associated with the amplified planetary wave structures reinforces – or in the case of the Indian duct, creates – the westerly ducts. Indeed it is certainly possible that as the westerly wind speeds increase along the equator in association with the material PV deformations that more synoptic scale wave trains will be able to propagate towards the equator from the Southern Hemisphere and thus break and contribute to the PV intrusion anomalies in our composites. However, a close inspection of the PV deformations associated with the large scale planetary waves during SSWs (not shown) reveals that the westerly wind perturbation resulting from the PV deformations only extends as far south as $\sim$5°N. Thus some other process must be taking place that induces the increased westerly winds deep into the Southern Hemisphere (Fig. 1b), which in turn contributes to the SH anomalies of PV (Fig. 5) and OLR (Fig. 14). One obvious candidate is a secondary tropical wave response that is initiated by the impending NH PV intrusions as suggested by Kiladis and Wheeler

(1995) and Kiladis (1998). A second possibility is that the intertial instability hypothesis that O'Sullivan and Hitchman (1992) applied to the lower mesosphere also operates in the UTLS. Regardless of the mechanism responsible for the hemispheric symmetry of the intrusions, it will be important to determine whether their existence and apparent connection to SSWs might provide a connection between NH dynamic variability and the variability of convection and transport in the Southern Hemisphere.

Acknowledgments.

We appreciate the careful and constructive comments from three anonymous reviewers that contributed to improving the content and presentation of the manuscript. This work was supported by the NSF Atmospheric and Geospace Science Postdoctoral Fellowship program (JRA). The authors thank Maria Gehne and David Allured for preparation and archiving of the ERA-Interim data that was originally provided by NCAR.

REFERENCES

Abatzoglou, J. T. and G. Magnusdottir, 2006: Planetary wave breaking and nonlinear reflection: Seasonal cycle and interannual variability. *J. Climate*, **19 (23)**, 6139–6152.

Albers, J. R. and T. Birner, 2014: Vortex preconditioning due to planetary and gravity waves prior to sudden stratospheric warmings. *J. Atmos. Sci.*, **71 (11)**, 4028–4054.

Appenzeller, C., H. Davies, and W. Norton, 1996: Fragmentation of stratospheric intrusions. *J. Geophys. Res.*, **101 (D1)**, 1435–1456.

Baldwin, M. P. and T. J. Dunkerton, 1999: Propagation of the Arctic Oscillation from the stratosphere to the troposphere. *J. Geophys. Res.*, **104 (D24)**, 30 937–30 946.

Baldwin, M. P. and T. J. Dunkerton, 2001: Stratospheric harbingers of anomalous weather regimes. *Science*, **294 (5542)**, 581–584.

Barnes, E. A. and D. L. Hartmann, 2011: Rossby wave scales, propagation, and the variability of eddy-driven jets. *J. Atmos. Sci.*, **68 (12)**, 2893–2908.

Branstator, G., 1995: Organization of storm track anomalies by recurring low-frequency circulation anomalies. *J. Atmos. Sci.*, **52 (2)**, 207–226.

Butler, A., D. Seidel, S. Hardiman, N. Butchart, T. Birner, and A. Match, 2014: Defining sudden stratospheric warmings. *Bull. Amer. Met. Soc.*, In press.

Cai, M., 2003: Potential vorticity intrusion index and climate variability of surface temperature. *Geophys. Res. Lett.*, **30 (3)**.

Cai, M. and H. M. van den Dool, 1991: Low-frequency waves and traveling storm tracks. Part I: Barotropic component. *J. Atmos. Sci.*, **48 (11)**, 1420–1436.

Charlton, A. J., A. O'Neill, W. Lahoz, and A. Massacand, 2004: Sensitivity of tropospheric forecasts to stratospheric initial conditions. *Quart. J. R. Met. Soc.*, **130 (600)**, 1771–1792.

Charlton, A. J. and L. M. Polvani, 2007: A new look at stratospheric sudden warmings. Part I: Climatology and modeling benchmarks. *J. Climate*, **20 (3)**, 449–469.

Cooper, O., et al., 2005: Direct transport of midlatitude stratospheric ozone into the lower troposphere and marine boundary layer of the tropical Pacific Ocean. *J. Geophys. Res.*, **110 (D23)**.

Dee, D. P., et al., 2011: The ERA-Interim reanalysis: Configuration and performance of the data assimilation system. *Quart. J. R. Met. Soc.*, **137**, 553–597.

Dias, J., S. Tulich, and G. Kiladis, 2012: An object based approach to assessing tropical convection organization. *J. Atmos. Sci*, **69**, 2488–2504.

Esler, J. and N. J. Matthewman, 2011: Stratospheric sudden warmings as self-tuning resonances. Part II: Vortex displacement events. *J. Atmos. Sci.*, **68 (11)**, 2505–2523.

Esler, J. and R. Scott, 2005: Excitation of transient rossby waves on the stratospheric polar vortex and the barotropic sudden warming. *J. Atmos. Sci.*, **62 (10)**, 3661–3682.

European Centre for Medium-Range Weather Forecasts, 2009: ERA-Interim Project. Research Data Archive at the National Center for Atmospheric Research, Computational and Information Systems Laboratory Boulder, CO. http://dx.doi.org/10.5065/D6CR5RD9 Accessed 12 May 2014.

Frederiksen, J. S. and P. J. Webster, 1988: Alternative theories of atmospheric teleconnections and low-frequency fluctuations. *Rev. Geophys.*, **26 (3)**, 459–494.

Funatsu, B. M. and D. W. Waugh, 2008: Connections between potential vorticity intrusions and convection in the eastern tropical Pacific. *J. Atmos. Sci.*, **65 (3)**, 987–1002.

Garfinkel, C. I., S. B. Feldstein, D. W. Waugh, C. Yoo, and S. Lee, 2012: Observed connection between stratospheric sudden warmings and the Madden-Julian Oscillation. *Geophys. Res. Lett.*, **39 (18)**.

Gettelman, A., P. Hoor, L. Pan, W. Randel, M. Hegglin, and T. Birner, 2011: The extratropical upper troposphere and lower stratosphere. *Rev. Geophys.*, **49 (3)**.

Hitchman, M. H. and A. S. Huesmann, 2007: A seasonal climatology of Rossby wave breaking in the 320-2000-k layer. *J. Atmos. Sci.*, **64 (6)**, 1922–1940.

Hoerling, M. P., T. K. Schaack, and A. J. Lenzen, 1991: Global objective tropopause analysis. *Mon. Wea. Rev.*, **119 (8)**, 1816–1831.

Hoskins, B. J. and T. Ambrizzi, 1993: Rossby wave propagation on a realistic longitudinally varying flow. *J. Atmos. Sci.*, **50 (12)**, 1661–1671.

Hoskins, B. J. and D. J. Karoly, 1981: The steady linear response of a spherical atmosphere to thermal and orographic forcing. *J. Atmos. Sci.*, **38 (6)**, 1179–1196.

Hsu, H.-H. and S.-H. Lin, 1992: Global teleconnections in the 250-mb streamfunction field during the Northern Hemisphere winter. *Mon. Wea. Rev.*, **120 (7)**, 1169–1190.

Hsu, J., M. J. Prather, and O. Wild, 2005: Diagnosing the stratosphere-to-troposphere flux of ozone in a chemistry transport model. *J. Geophys. Res.*, **110 (D19)**.

Jin, F., L. Pan, and M. Watanabe, 2006: Dynamics of synoptic eddy and low-frequency flow interaction. Part I: A linear closure. *J. Atmos. Sci.*, **63 (7)**, 1677–1694.

Karoly, D. J. and B. J. Hoskins, 1982: Three dimensional propagation of planetary waves. *J. Met. Soc. Jap.*, **60**, 109–123.

Kiladis, G. N., 1998: Observations of Rossby waves linked to convection over the eastern tropical Pacific. *J. Atmos. Sci.*, **55 (3)**, 321–339.

Kiladis, G. N. and K. M. Weickmann, 1992: Extratropical forcing of tropical Pacific convection during northern winter. *Mon. Wea. Rev.*, **120 (9)**, 1924–1939.

Kiladis, G. N. and M. Wheeler, 1995: Horizontal and vertical structure of observed tropospheric equatorial Rossby waves. *J. Geophys. Res.*, **100 (D11)**, 22 981–22 997.

Kim, J., W. J. Randel, T. Birner, and M. Abalos, 2015: Spectrum of wave forcing associated with the annual cycle of upwelling at the tropical tropopause. *submitted to J. Atmos. Sci.*

Kodera, K., 2006: Influence of stratospheric sudden warming on the equatorial troposphere. *Geophys. Res. Lett.*, **33 (6)**.

Kodera, K., N. Eguchi, J. N. Lee, Y. Kuroda, and S. Yukimoto, 2011: Sudden changes in the tropical stratospheric and tropospheric circulation during January 2009. *J. Met. Soc. Jap.*, **89 (3)**, 283–290.

Kuroda, Y., 2008: Effect of stratospheric sudden warming and vortex intensification on the tropospheric climate. *J. Geophys. Res.*, **113 (D15)**.

Kuttippurath, J. and G. Nikulin, 2012: A comparative study of the major sudden stratospheric warmings in the Arctic winters 2003/2004–2009/2010. *Atmos. Chem. Phys.*, **12 (17)**, 8115–8129.

Lait, L. R., 1994: An alternative form for potential vorticity. *J. Atmos. Sci.*, **51 (12)**, 1754–1759.

Langford, A., et al., 2014: An overview of the 2013 Las Vegas Ozone Study (LVOS): Impact of stratospheric intrusions and long-range transport on surface air quality. *Atm. Environment.*

Leblanc, T., I. S. McDermid, and A. Hauchecorne, 2004: A study of ozone variability and its connection with meridional transport in the northern Pacific lower stratosphere during summer 2002. *J. Geophys. Res.*, **109 (D11)**.

Lee, S., 1999: Why are the climatological zonal winds easterly in the equatorial upper troposphere? *J. Atmos. Sci.*, **56 (10)**, 1353–1363.

Liebmann, L. and C. Smith, 1996: Description of a complete (interpolated) outgoing longwave radiation dataset. *Bull. Amer. Met. Soc.*, **77(6)**, 1275–1277.

Limpasuvan, V., D. W. Thompson, and D. L. Hartmann, 2004: The life cycle of the northern hemisphere sudden stratospheric warmings. *J. Atmos. Sci.*, **17**, 2584–2596.

Liu, C., B. Tian, K.-F. Li, G. L. Manney, N. J. Livesey, Y. L. Yung, and D. E. Waliser, 2014: Northern Hemisphere mid-winter vortex-displacement and vortex-split stratospheric sudden warmings: Influence of the Madden-Julian Oscillation and Quasi-Biennial Oscillation. *J. Geophys. Res.J*, **119**.

Manney, G. L., et al., 2009: Aura microwave limb sounder observations of dynamics and transport during the record-breaking 2009 Arctic stratospheric major warming. *Geophys. Res. Lett.*, **36 (12)**, L12 815.

Martineau, P. and S.-W. Son, 2013: Planetary-scale wave activity as a source of varying tropospheric response to stratospheric sudden warming events: A case study. *J. Geophys. Res.*, **118 (19)**, 10–994.

Matthewman, N. J. and J. Esler, 2011: Stratospheric sudden warmings as self-tuning resonances. Part I: Vortex splitting events. *J. Atmos. Sci.*, **68 (11)**, 2481–2504.

Matthewman, N. J., J. G. Esler, A. J. Charlton-Perez, and L. Polvani, 2009: A new look at stratospheric sudden warmings. Part III: Polar vortex evolution and vertical structure. *J. Climate*, **22 (6)**, 1566–1585.

McInturff, R. M., 1978: Stratospheric warmings: Synoptic, dynamic, and general circulation aspects. NASA Ref. Publ. 1017, 166pp.

McIntyre, M., 1982: How well do we understand the dynamics of stratospheric warmings? *J. Met. Soc. Jap.*, **60 (1)**, 37–65.

McIntyre, M. and T. Palmer, 1983: Breaking planetary waves in the stratosphere. *Nature*, **305 (5935)**, 593–600.

Müller, R. and G. Günther, 2003: A generalized form of Lait's modified potential vorticity. *J. Atmos. Sci.*, **60 (17)**, 2229–2237.

Munchak, L. A. and L. L. Pan, 2014: Separation of the lapse rate and the cold point tropopauses in the tropics and the resulting impact on cloud top-tropopause relationships. *J. Geophys. Res.*, **119 (13)**, 7963–7978.

Murakami, T. and M. S. Unninayar, 1977: Atmospheric circulation during December 1970 through February 1971. *Mon. Wea. Rev.*, **105 (8)**, 1024–1038.

Nash, E. R., P. A. Newman, J. E. Rosenfield, and M. R. Schoeberl, 1996: An objective determination of the polar vortex using Ertel's potential vorticity. *J. Geophys. Res.*, **101 (D5)**, 9471–9478.

Nath, D., S. Sridharan, S. Sathishkumar, S. Gurubaran, and W. Chen, 2013: Lower stratospheric gravity wave activity over Gadanki (13.5° N, 79.2° E) during the stratospheric sudden warming of 2009: Link with potential vorticity intrusion near Indian sector. *J. Atmos. Sol.-Terr. Phy.*, **94**, 54–64.

O'Sullivan, D. J. and M. H. Hitchman, 1992: Inertial instability and Rossby wave breaking in a numerical model. *J. Atmos. Sci.*, **49 (12)**, 991–1002.

Polvani, L. M. and R. Saravanan, 2000: The three-dimensional structure of breaking Rossby waves in the polar wintertime stratosphere. *J. Atmos. Sci.*, **57 (21)**, 3663–3685.

Postel, G. A. and M. H. Hitchman, 1999a: A climatology of Rossby wave breaking along the subtropical tropopause. *J. Atmos. Sci.*, **56 (3)**, 359–373.

Postel, G. A. and M. H. Hitchman, 1999b: A climatology of Rossby wave breaking along the subtropical tropopause. *J. Atmos. Sci.*, **56 (3)**, 359–373.

Randel, W. J. and E. J. Jensen, 2013: Physical processes in the tropical tropopause layer and their roles in a changing climate. *Nature Geoscience*, **6 (3)**, 169–176.

Resmi, E., K. Mohanakumar, and K. Appu, 2013: Effect of polar sudden stratospheric warming on the tropical stratosphere and troposphere and its surface signatures over the Indian region. *J. Atmos. Sol.-Terr. Phy.*, **105**, 15–29.

Riehl, H., 1954: Tropical meteorology. McGraw-Hill, New York, 392 pp.

Sardeshmukh, P. D. and B. J. Hoskins, 1988: The generation of global rotational flow by steady idealized tropical divergence. *J. Atmos. Sci.*, **45 (7)**, 1228–1251.

Sathishkumar, S. and S. Sridharan, 2011: Observations of 2–4 day inertia-gravity waves from the equatorial troposphere to the f region during the sudden stratospheric warming event of 2009. *J. Geophys. Res.*, **116 (A12)**.

Schoeberl, M. R., 1978: Stratospheric warmings: Observations and theory. *Reviews of Geophysics*, **16 (4)**, 521–538.

Scott, R. and J. Cammas, 2002: Wave breaking and mixing at the subtropical tropopause. *J. Atmos. Sci.*, **59 (15)**, 2347–2361.

Scott, R., J.-P. Cammas, P. Mascart, and C. Stolle, 2001: Stratospheric filamentation into the upper tropical troposphere. *J. Geophys. Res.*, **106 (D11)**, 11 835–11 848.

Scott, R. and L. Polvani, 2006: Internal variability of the winter stratosphere. part i: Time-independent forcing. *J. Atmos. Sci.*, **63 (11)**, 2758–2776.

Sherwood, S., R. Roca, T. Weckwerth, and N. Andronova, 2010: Tropospheric water vapor, convection, and climate. *Rev. Geophys.*, **48 (2)**.

Sridharan, S. and S. Sathishkumar, 2011: Observational evidence of deep convection over Indonesian sector in relation with major stratospheric warming events of 2003–04 and 2005–06. *J. Atmos. Sol.-Terr. Phy.*, **73 (17)**, 2453–2461.

Starr, V. P., 1948: An essay on the general circulation of the Earth's atmosphere. *J. Meteor.*, **5 (2)**, 39–43.

Thompson, D. W. and J. M. Wallace, 1998: The Arctic Oscillation signature in the wintertime geopotential height and temperature fields. *Geophys. Res. Lett.*, **25 (9)**, 1297–1300.

Thompson, D. W. and J. M. Wallace, 2000: Annular modes in the extratropical circulation. Part I: month-to-month variability. *J. Climate*, **13 (5)**, 1000–1016.

Thompson, D. W. and J. M. Wallace, 2001: Regional climate impacts of the northern hemisphere annular mode. *Science*, **293 (5527)**, 85–89.

Thurairajah, B., R. L. Collins, V. L. Harvey, R. S. Lieberman, M. Gerding, K. Mizutani, and J. M. Livingston, 2010: Gravity wave activity in the Arctic stratosphere and mesosphere during the 2007–2008 and 2008–2009 stratospheric sudden warming events. *J. Geophys. Res.*, **115 (D3)**.

Tomas, R. A. and P. J. Webster, 1994: Horizontal and vertical structure of cross-equatorial wave propagation. *J. Atmos. Sci.*, **51 (11)**, 1417–1430.

Tsidu, G. M. and K. Ture, 2013: Mechanisms of ozone enhancement during stratospheric intrusion coupled with convection over upper troposphere equatorial Africa. *Atm. Environment*, **70**, 410–424.

Waugh, D. W., 2005: Impact of potential vorticity intrusions on subtropical upper tropospheric humidity. *J. Geophys. Res.*, **110 (D11)**.

Waugh, D. W. and B. M. Funatsu, 2003: Intrusions into the tropical upper troposphere: Three-dimensional structure and accompanying ozone and OLR distributions. *J. Atmos. Sci.*, **60 (4)**, 637–653.

Waugh, D. W. and L. M. Polvani, 2000: Climatology of intrusions into the tropical upper troposphere. *Geophys. Res. Lett.*, **27 (23)**, 3857–3860.

Waugh, D. W. and L. M. Polvani, 2010: *Stratospheric polar vortices*, Vol. 190 Geophysical Monograph Series. American Geophysical Union, 43–57 pp.

Webster, P. J. and J. R. Holton, 1982: Cross-equatorial response to middle-latitude forcing in a zonally varying basic state. *J. Atmos. Sci.*, **39 (4)**, 722–733.

Wheeler, M. C. and H. H. Hendon, 2004: An all-season real-time multivariate MJO index: Development of an index for monitoring and prediction. *Mon. Wea. Rev.*, **132 (8)**, 1917–1932.

Yoshida, K. and K. Yamazaki, 2011: Tropical cooling in the case of stratospheric sudden warming in January 2009: Focus on the tropical tropopause layer. *Atmos. Chem. Phys.*, **11 (13)**, 6325–6336.

List of Figures

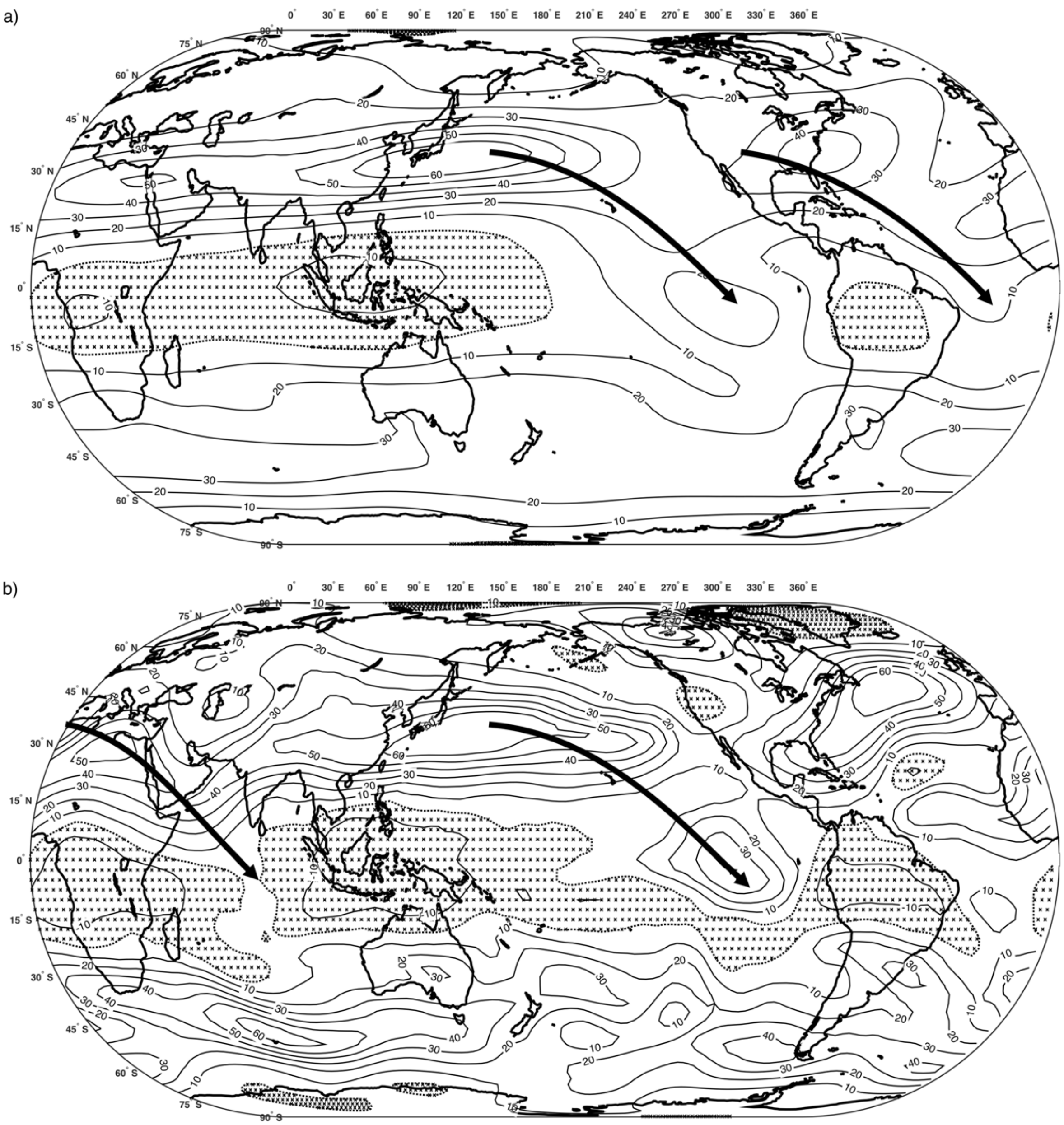

FIG. 1. Time averaged zonal wind (ms^{-1}) on the 350 K isentropic surface for (a) DJF between 1979-2012 and (b) 16-22 January 2009. The stippling denotes regions of easterly wind, while the thick black arrows denote great circle paths that approximate barotropic wave train pathways along the waveguides described in the Introduction.

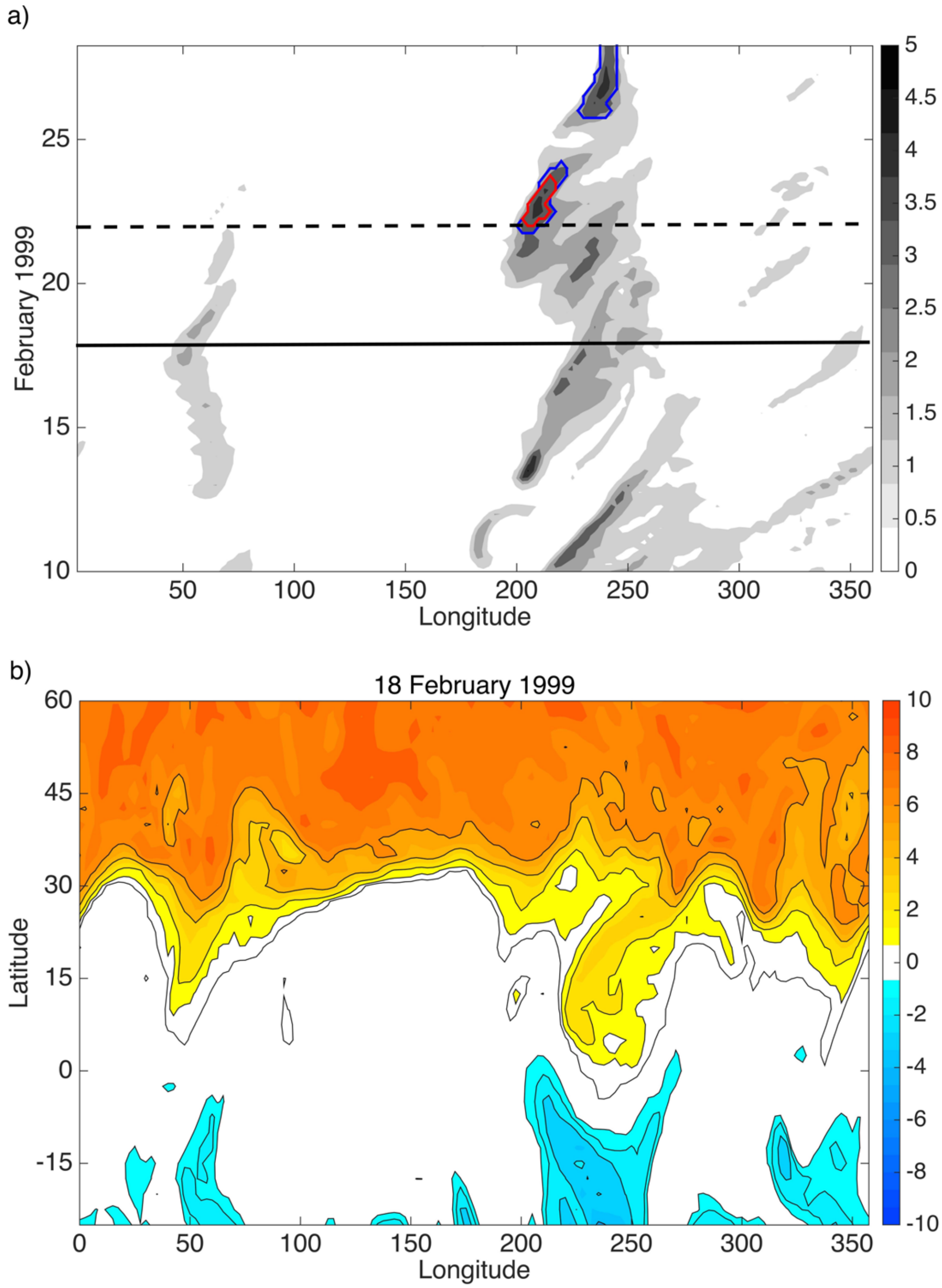

Fig. 2. Potential vorticity (PVU) on the 350 K isentropic surface for (a) 10-28 February 1999 at 15° N and (b) 18 February 1999. In (a) the red contours enclose PV intrusions that exceed the 3.75 PVU threshold, the blue contours enclose intrusions that exceed the 3.15 PVU threshold, the horizontal dashed black line denotes the central warming date for the 22 February split SSW, and the solid black line denotes the date for the corresponding latitude-longitude cross section shown in (b). The black contours overlaying (b) denote the +/- 0.5, 1, 2, 4, and 6 PVU isolevels.

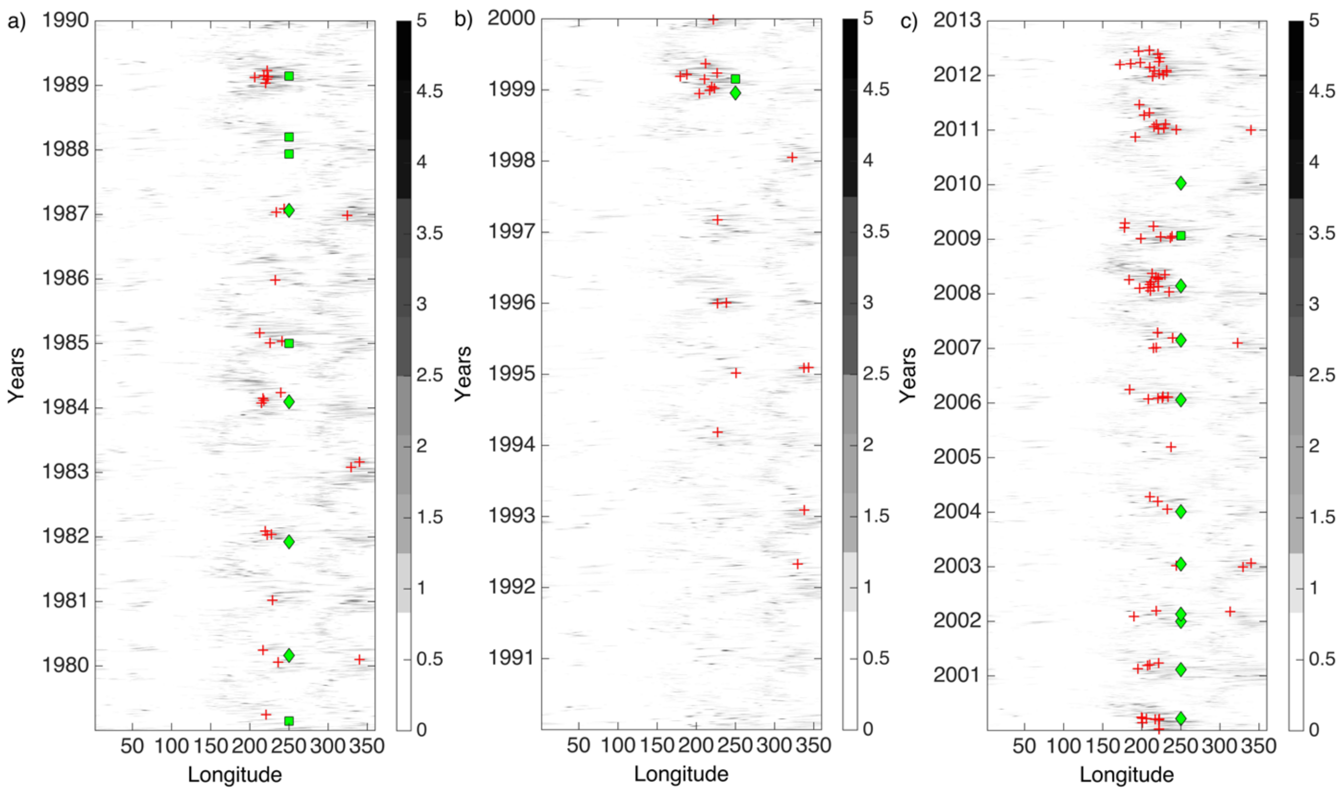

Fig. 3. Potential vorticity (PVU) on the 350 K isentropic surface at 15° N for the years (a) 1979-1989, (b) 1990-1999, and (c) 2000-2012. The centroid of each of the 128 PV intrusions between 1979-2012 that exceed the 3.75 PVU threshold are denoted by a red + symbol. The central warming dates of displacement and split SSWs are denoted by green diamonds and squares, respectively.

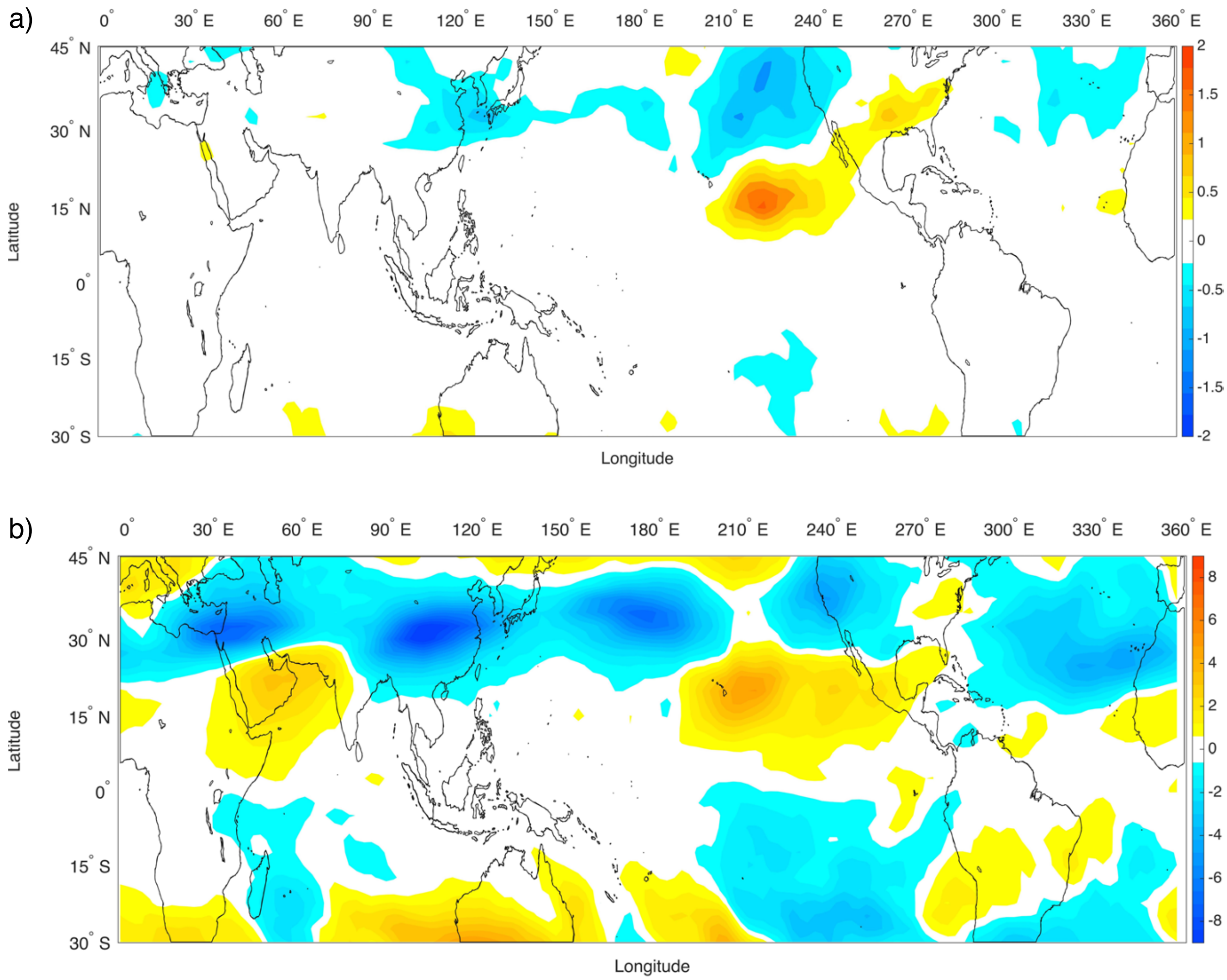

Fig. 4. Time averaged composite potential vorticity (PVU) anomalies on the 350 K isentrope for the time periods (a) that exceed the 3.75 PVU threshold for 1979-2012, and (b) two weeks before and after (4 weeks total) the central warming date for all SSWs between 1979-2012. Note that the contour scales of (a) and (b) are markedly different and that the units of the composites are 10^{-1} PVU instead of PVU because there is some spatial variability in the exact location where each individual wave breaks within the westerly ducts.

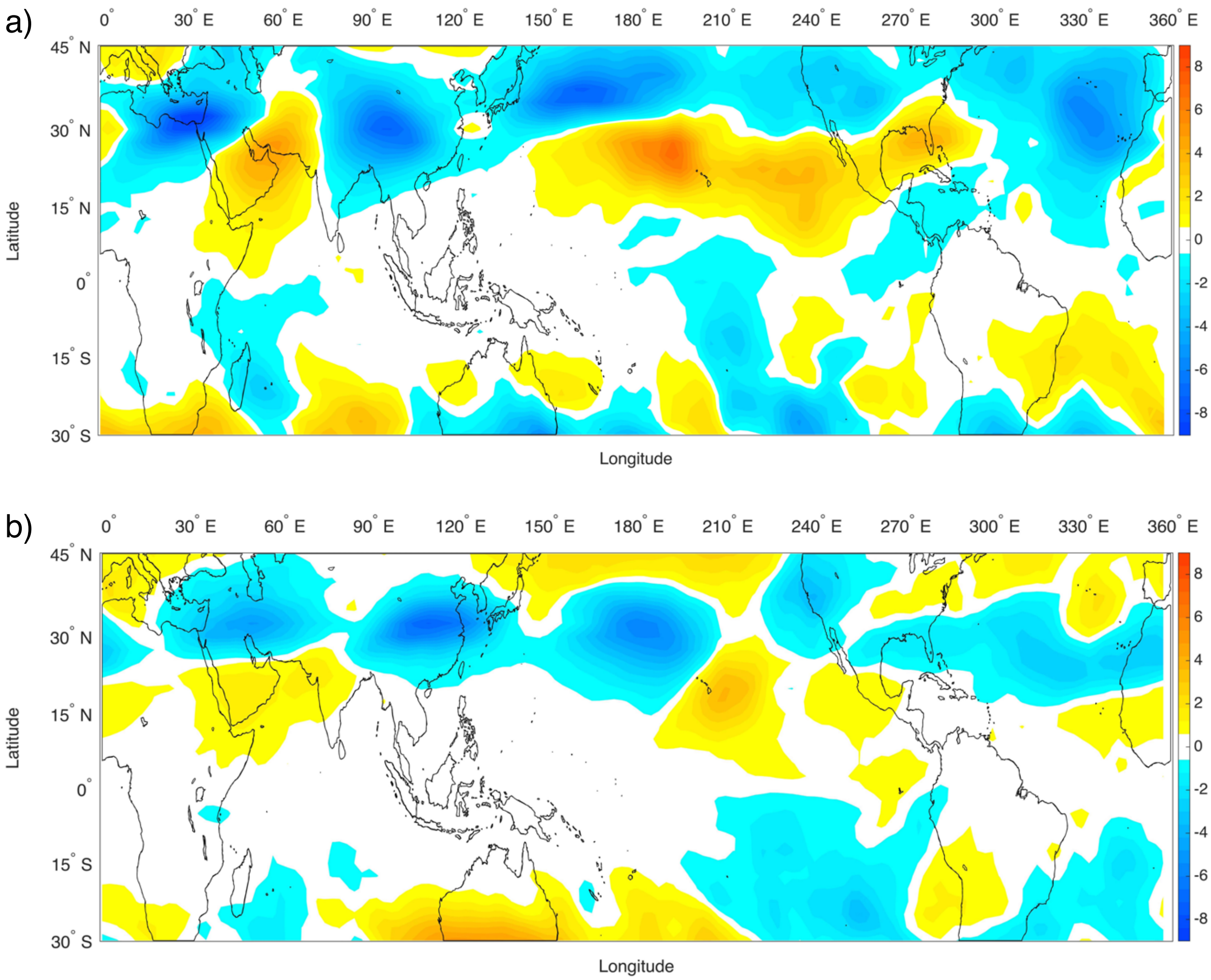

Fig. 5. Composite potential vorticity (PVU) anomalies on the 350 K isentrope time averaged over the two weeks before and after the central warming date for (a) split SSWs and (b) displacement SSWs between 1979-2012. The units in both figures are 10^{-1} PVU.

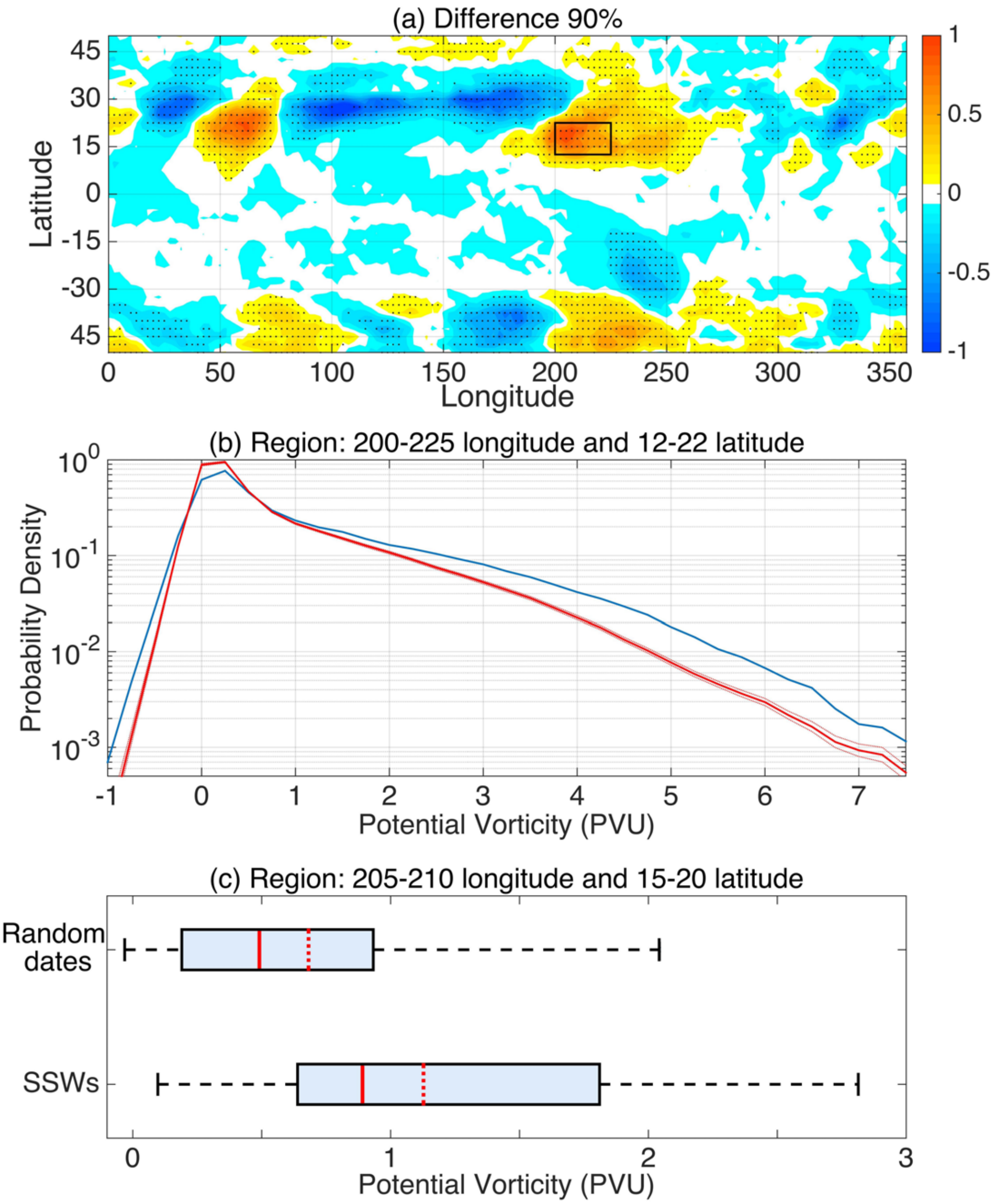

FIG. 6. (a) Difference in the 90^{th} percentile between the PDF of PV on the 350 K isentrope for the two weeks before the central warming date for all SSWs and the PDF for the 2,200 randomly selected two week periods (see text for details). In (a), the stippling indicates regions where the magnitude of the anomaly lies outside of the boundaries of the 95^{th} percentile bootstrap confidence interval of the climatological PDF. (b) PDF for the two weeks prior to all SSWs (blue line) and randomly selected two week periods (red line) with 95^{th} percentile bootstrap confidence interval (dashed red lines) for the region in the latitude-longitude plane enclosed by the black box in (a). (c) The 25^{th}-75^{th} percentiles (blue boxes), medians (vertical red lines), means (vertical red dotted lines), and extrema (vertical black lines) for the two weeks prior to the randomly selected periods (top) and for all SSWs (bottom) for the region between 205°-210° and 15°-20° N.

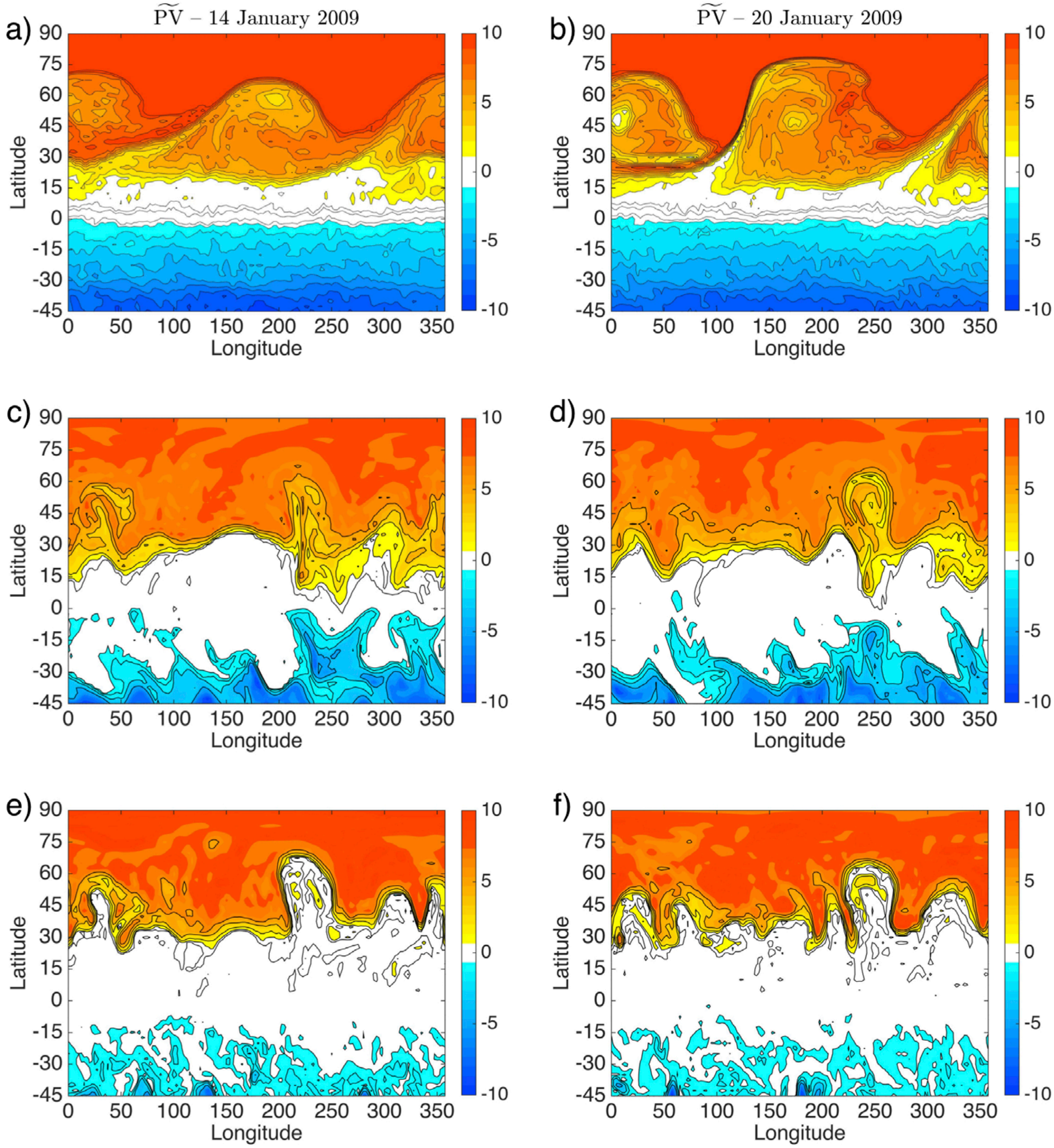

FIG. 7. Modified potential vorticity ($\widetilde{\mathrm{PV}}$) for 14 and 20 January 2009 (left and right column, respectively) on the 700 K (a and b), 350 K (c and d), and 320 K (e and f) isentropic surfaces. For the 700 K levels, dotted black lines are plotted between -10 and 10 $\widetilde{\mathrm{PVU}}$ in one $\widetilde{\mathrm{PVU}}$ increments. For the 320 and 350 K levels, solid black lines are plotted for the +/- 0.5, 1, 2, 4, and 6 $\widetilde{\mathrm{PVU}}$ isolevels. Modified potential vorticity is defined in the discussion of Fig. 8.

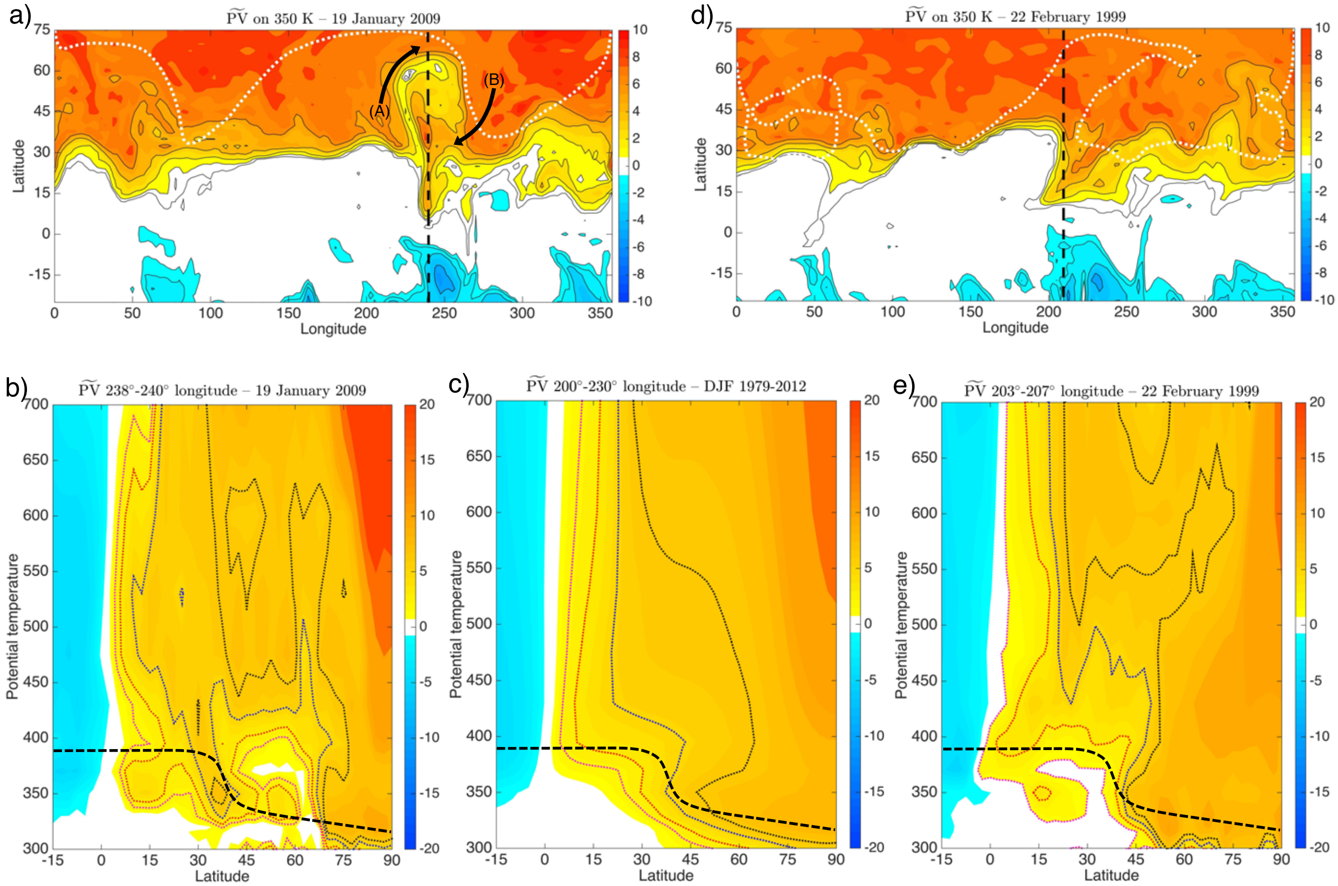

FIG. 8. Modified potential vorticity ($\widetilde{\mathrm{PV}}$ - see text for definition) on the 350 K isentrope with thin solid black lines denoting the +/- 0.5, 1, 2, 4, and 6 $\widetilde{\mathrm{PVU}}$ isolevels for: (a) 19 January 2009, and (d) 22 February 1999. In (a), the dotted white line denotes the 600 K isentropic surface 8.5 $\widetilde{\mathrm{PVU}}$ isolevel and the black curved arrows labeled (A) and (B) denote the sense of rotation of the breaking wave over the eastern Pacific region. In (d), the dotted white line denotes the 530 K isentropic surface 6.5 $\widetilde{\mathrm{PVU}}$ isolevel. The thick dotted black lines in (a) and (d) denote the cross sectional slices shown in (b) and (e). Cross sections of $\widetilde{\mathrm{PV}}$ for: (b) 19 January 2009 with 2, 3, 5, and 6.5 $\widetilde{\mathrm{PVU}}$ isolevels overlaid (pink, red, blue, and black dotted lines); (c) 1979-2012 DJF for the Pacific duct with 2, 3, 5, 6.5 $\widetilde{\mathrm{PVU}}$ isolevels overlaid (pink, red, blue, and black dotted lines); and (e) 22 February 1999 with 1, 3, 5, 6.5 $\widetilde{\mathrm{PVU}}$ isolevels overlaid (pink, red, blue, and black dotted lines). In (b), (c), and (e) a qualitative thermal tropopause, which is the same for each figure, is overlaid for visual reference (thick dashed black line) and the dotted lines are plotted in the same order – pink, red, blue, and black from equator to pole, respectively – in order to ease comparison between each figure.

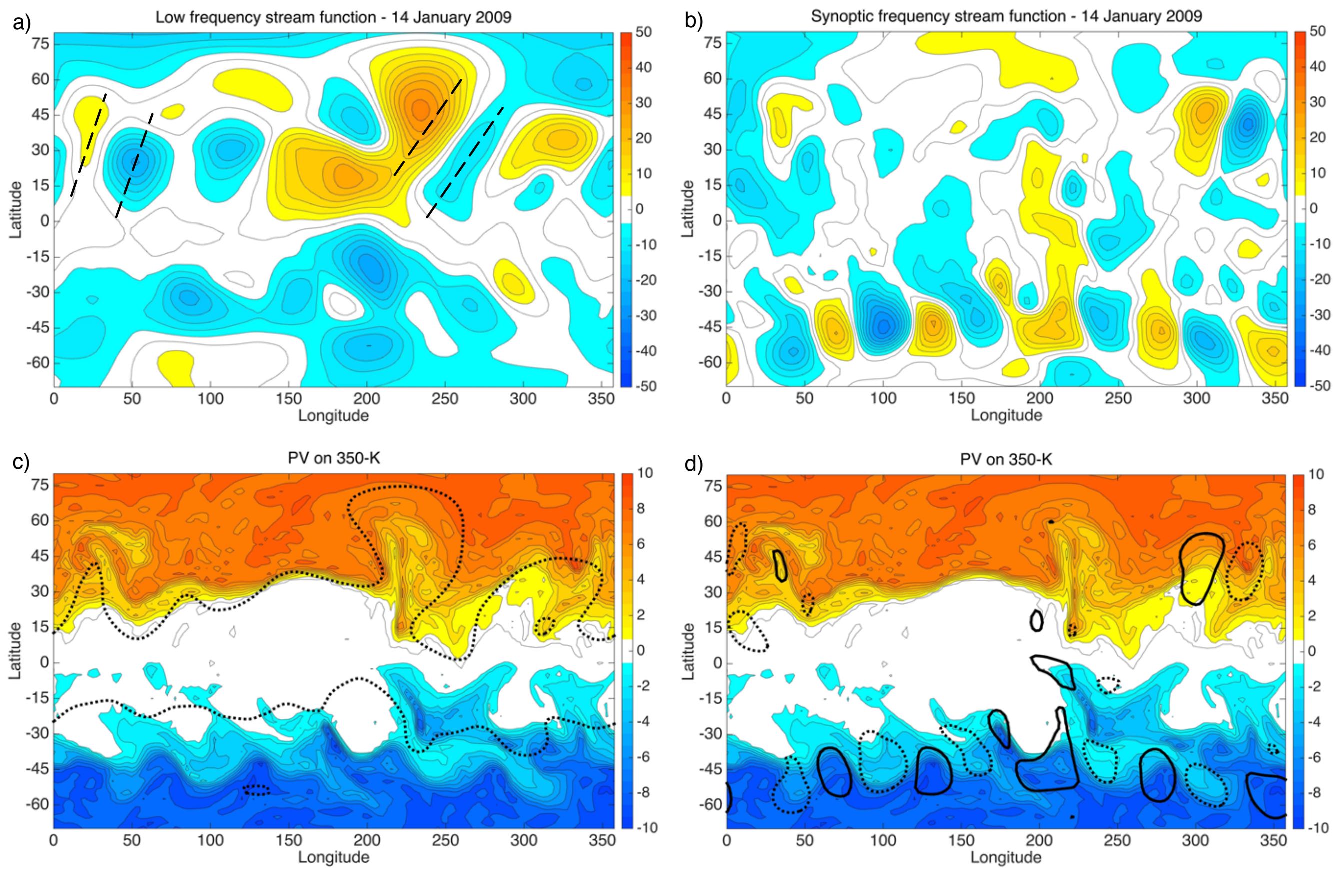

FIG. 9. 14 January 2009: (a) low-frequency (30-120 day filtered) stream function with black dashed lines denoting approximate wave tilt, (b) synoptic scale (1-10 day filtered) stream function, (c) PV with 30-365 day filtered zero stream function isolevel overlaid (dotted black line), and (d) PV with 1-10 day filtered -10 and 10 stream function isolevel overlaid (dotted and solid black lines, respectively). All figures are plotted on the 350 K isentropic surface. Units for the stream function are $10^{-6}\mathrm{m}^2\mathrm{s}^{-1}$ and PV is in units of PVU.

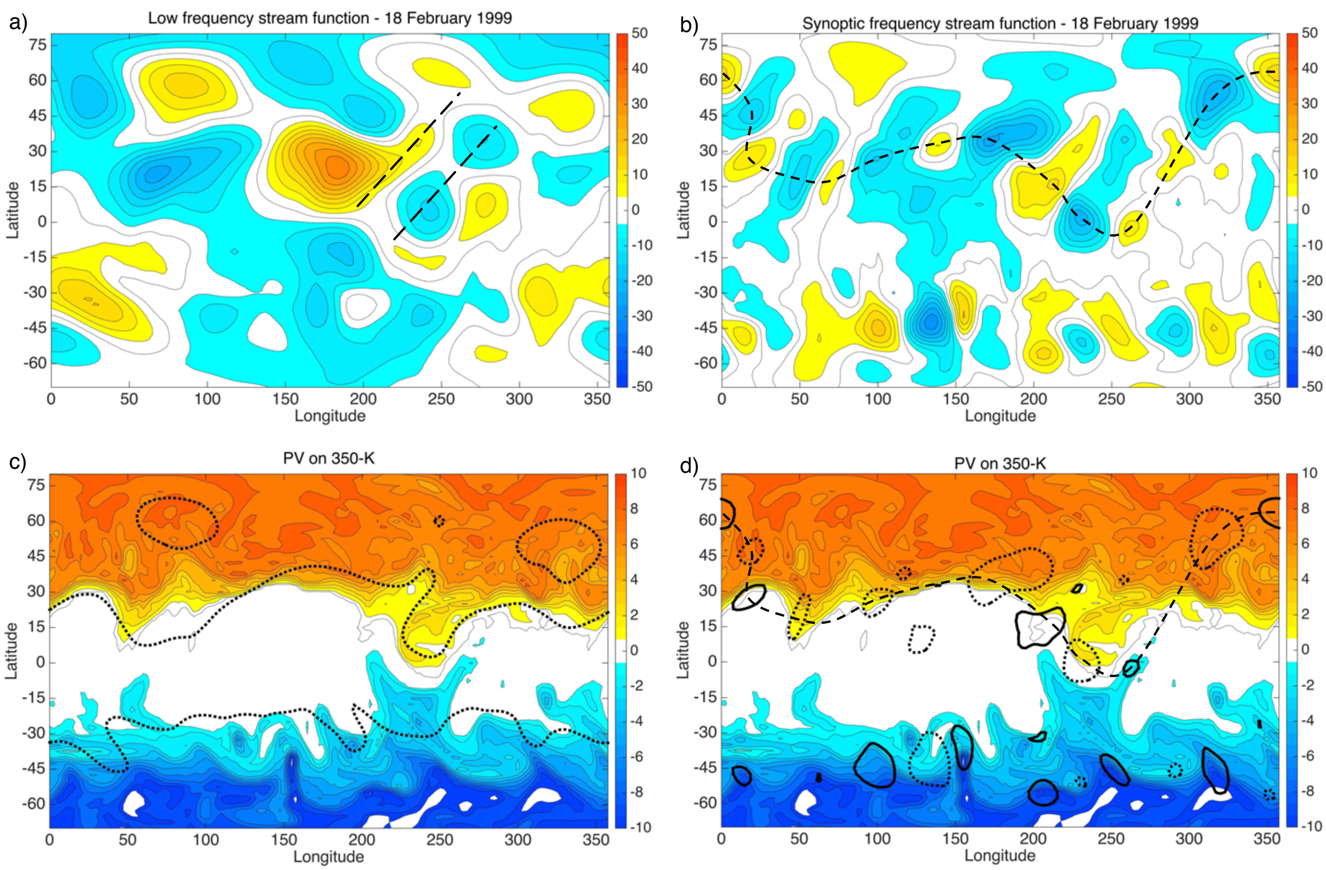

FIG. 10. 18 February 1999: (a) low-frequency (30-120 day filtered) stream function with black dashed lines denoting approximate wave tilt, (b) synoptic scale (1-10 day filtered) stream function, (c) PV with 30-365 day filtered zero stream function isolevel overlaid (dotted black line), and (d) PV with 1-10 day filtered -10 and 10 stream function isolevels overlaid (dotted and solid black lines, respectively). In (b) and (d), the dashed black line connects the maxima of the synoptic scale stream function wave train pattern in the NH, where the tilt of the synoptic waves is approximately perpendicular to this line. All figures are plotted on the 350 K isentropic surface. Units for the stream function are $10^{-6}\mathrm{m}^2\mathrm{s}^{-1}$ and PV is in units of PVU.

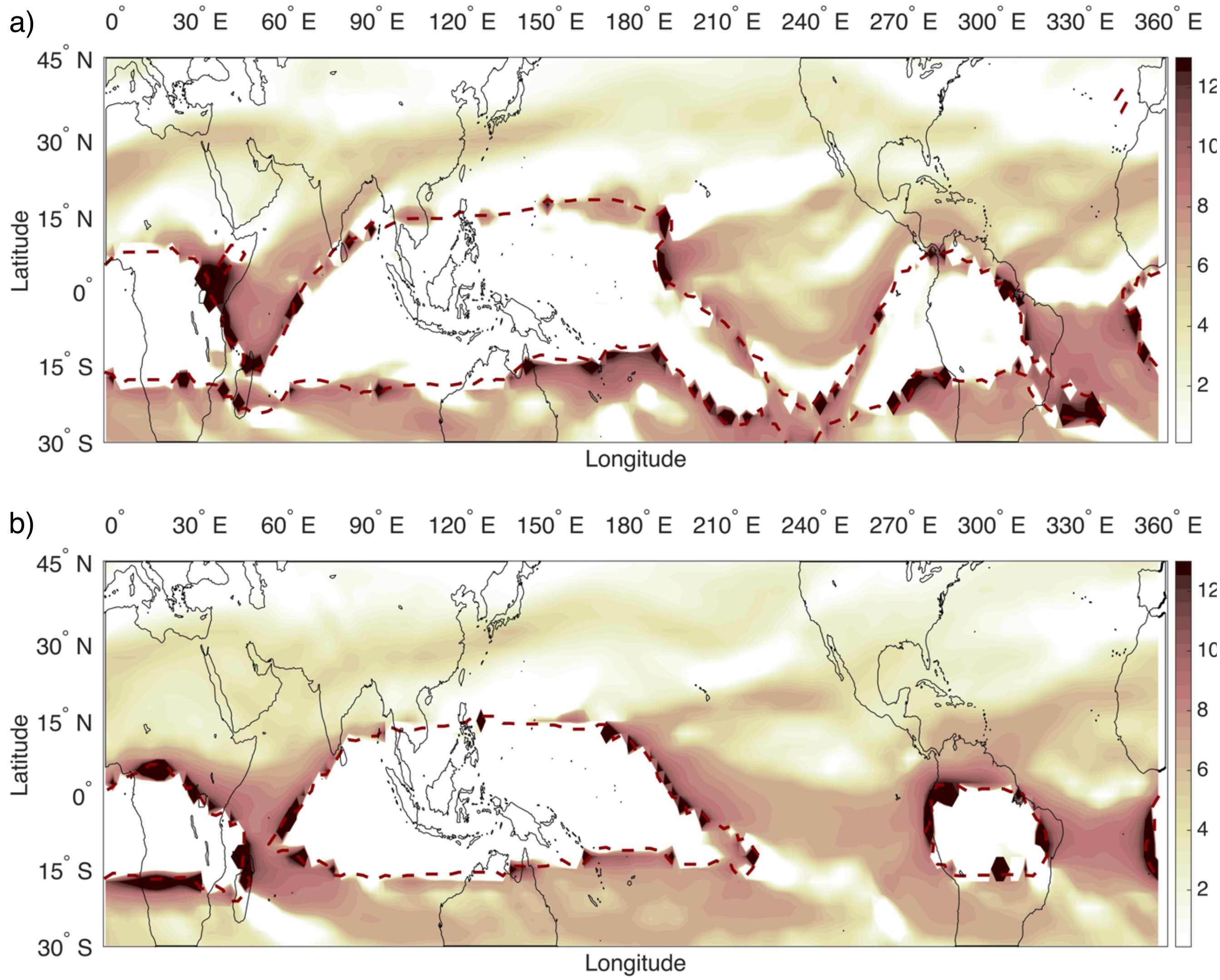

FIG. 11. Time averaged total stationary Rossby wavenumber squared (10^{-12} m^{-2}) on the 350 K isentropic surface for (a) 18-24 February 1999 and (b) the week periods prior to the 1985, 1987, 1988, 1999, and 2009 split SSWs. In (a) and (b) the dotted red line denotes where $u = 0$ ms^{-1}, which is the critical line for stationary Rossby waves.

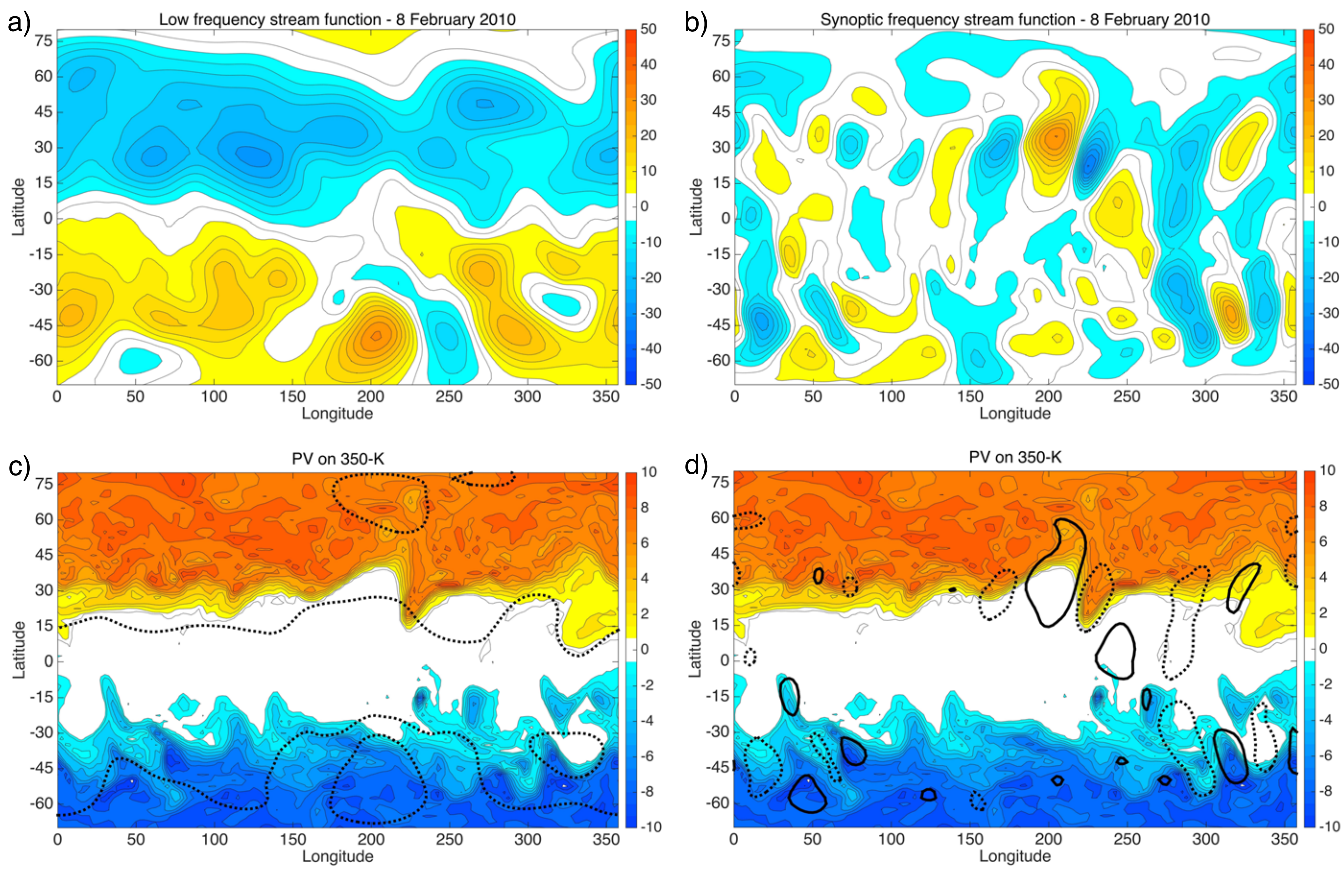

Fig. 12. 8 February 2010: (a) low-frequency (30-120 day filtered) stream function, (b) synoptic scale (1-10 day filtered) stream function, (c) PV with 30-365 day filtered zero stream function isolevel overlaid (dotted black line), and (d) PV with 1-10 day filtered -10 and 10 stream function isolevels overlaid (dotted and solid black lines, respectively). All figures are plotted on the 350 K isentropic surface. Units for the stream function are $10^{-6}\mathrm{m}^2\mathrm{s}^{-1}$ and PV is in units of PVU.

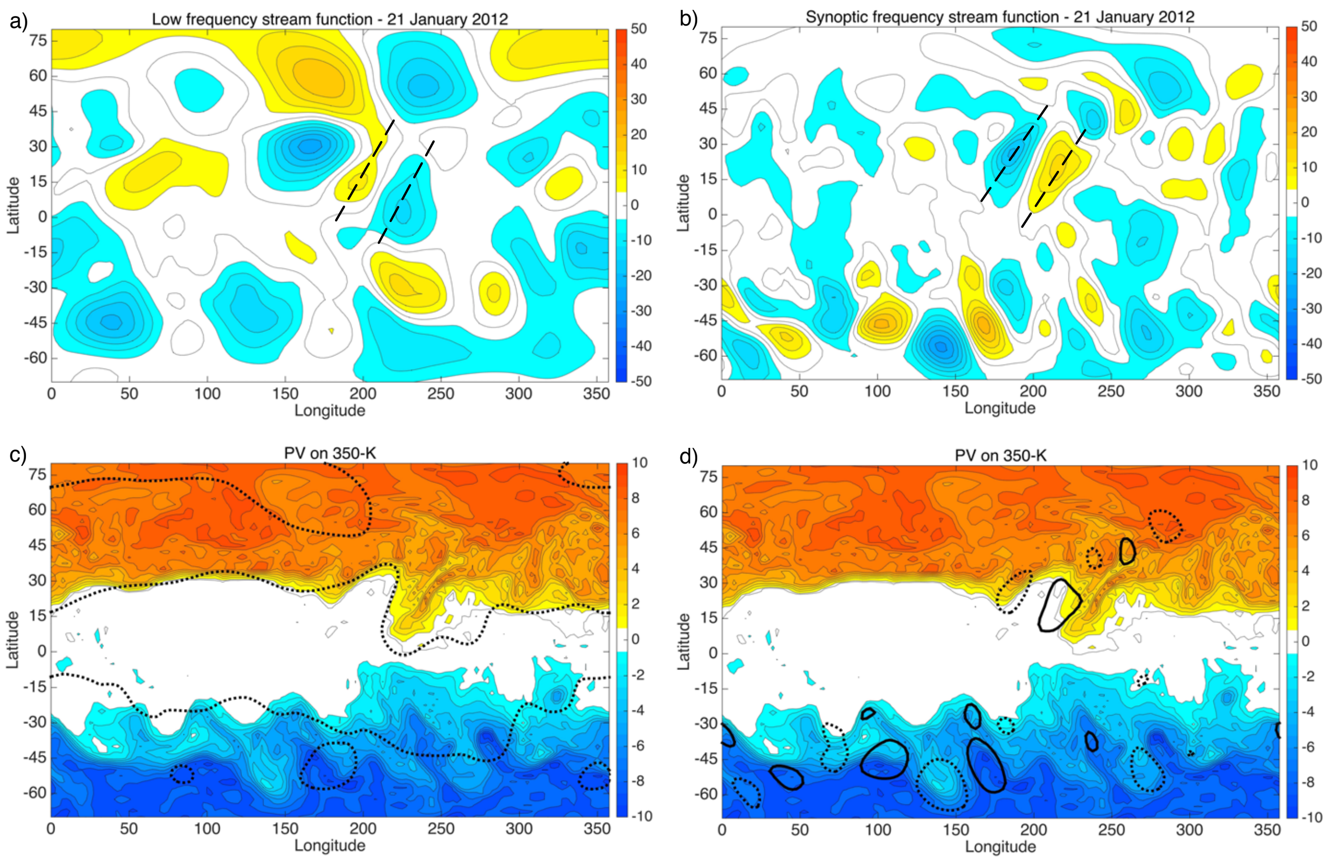

Fig. 13. 21 January 2012: (a) low-frequency (30-120 day filtered) stream function, (b) synoptic scale (1-10 day filtered) stream function, (c) PV with 30-365 day filtered zero stream function isolevel overlaid (dotted black line), and (d) PV with 1-10 day filtered -10 and 10 stream function isolevel overlaid (dotted and solid black lines, respectively). In (a) and (b), the black dashed lines denote the approximate wave tilt. All figures are plotted on the 350 K isentropic surface. Units for the stream function are $10^{-6}\mathrm{m}^2\mathrm{s}^{-1}$ and PV is in units of PVU.

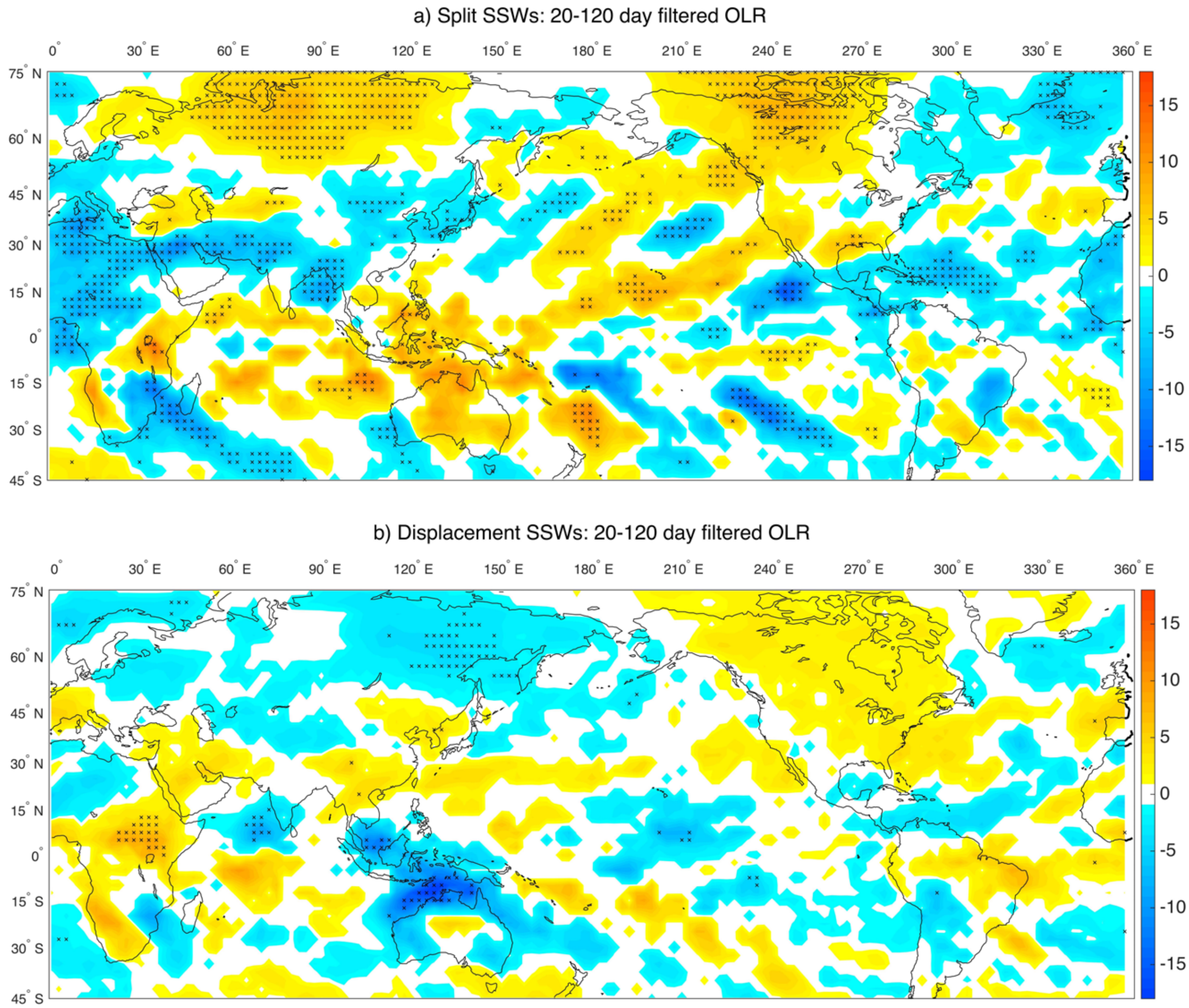

FIG. 14. 20-120 day filtered OLR composited over the 14 days prior to the central warming date for all (a) split and (b) displacement SSWs between 1979-2012. Anomalies are only plotted if they are significantly different from the DJF climatology at the 95% confidence level using a two-tailed Student's t-Test; stippling indicates where the anomaly is larger than 0.5 of a standard deviation of the DJF climatology where the standard deviation is computed at all points in latitude and longitude. Units for both figures are in W m^{-2} and colored, filled contours are only shown for values $\geq |2|$ W m^{-2}.

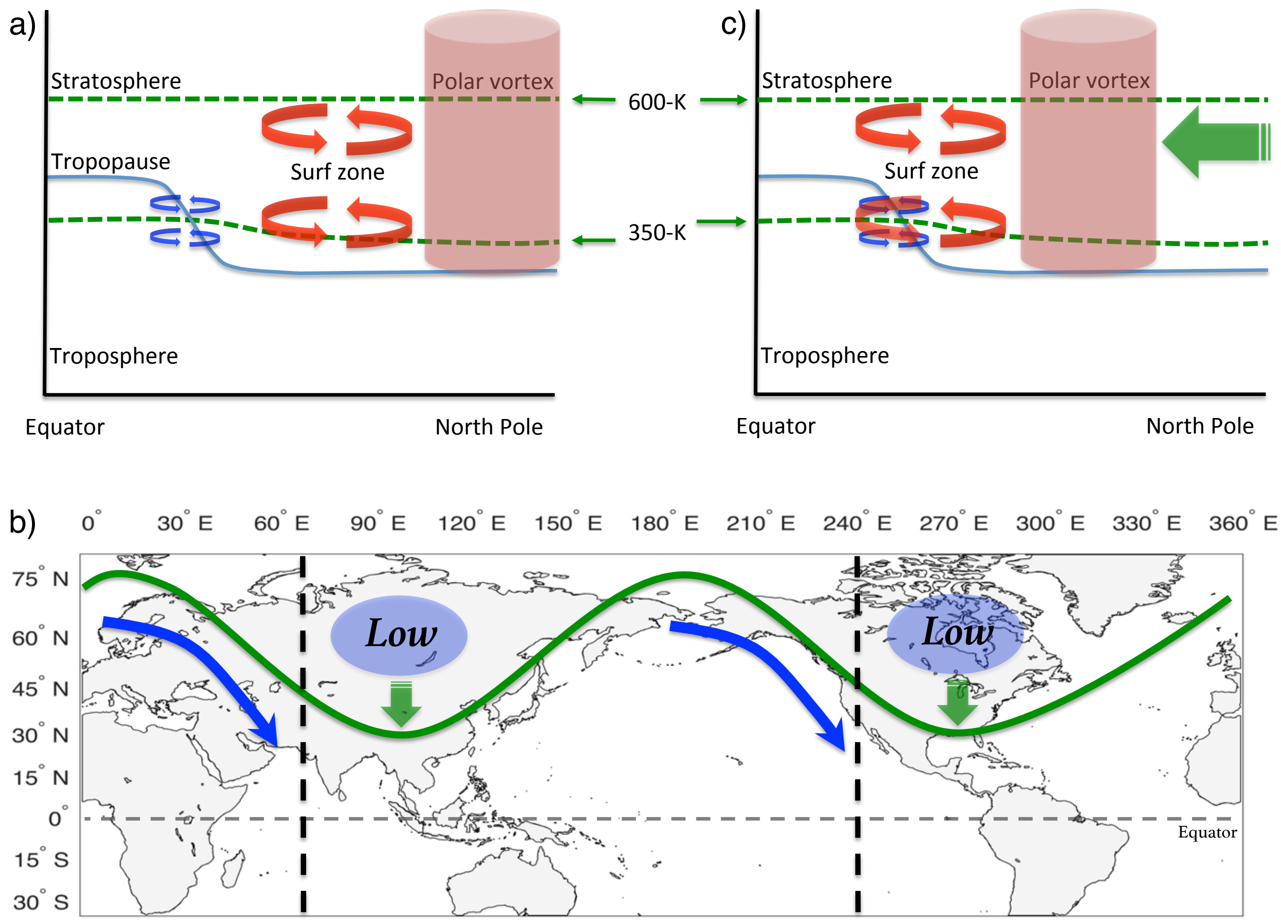

FIG. 15. Schematic diagram depicting the mechanisms we propose are responsible for the largest DJF PV intrusions. Part (a) depicts DJF climatological conditions with synoptic scale wave breaking along the subtropical tropopause (blue circular arrows) and planetary scale wave breaking fully contained in the stratosphere (red circular arrows); the location of the climatological tropopause is shown as the solid blue line, the polar vortex is depicted by the red cylinder, and the 350 and 600 K isentropic surfaces are shown as the dashed green lines. Part (b) depicts the situation along the 350 K isentropic surface during a split SSW where two daughter vortices move equatorward (thick green arrows) and cause a planetary scale PV deformation (solid green line). The thick dashed black lines in (b) denote the regions in the latitude-height plane that apply to the cross section in Part (c). Part (c) depicts conditions common during anomalously large planetary wave events (e.g. SSWs) where the stratospheric surf-zone is pushed equatorward and planetary wave breaking impinges upon the subtropical tropopause over a deep vertical layer of the UTLS (depicted by the red arrows); this is the effect of item (1) in the Conclusion section. The secondary effect of the PV deformation shown in (b) (i.e. item (2) in the Conclusion section) is the preferential ducting of synoptic scale wave trains along the blue arrows in Part (b).